POTENTIAL DRUGS CONTAINING AMINES AS REPRESENTATIVE EXAMPLE OF PHARMACEUTICAL AND BIOLOGICALLY ACTIVE COMPOUNDS

Abdou S.El-Tabl [1], Alla El-Sayed Amin [2], Ahmed M.Ashour[1], Mohammed H. H. Abu-Setta[*1] And Hager S.Wheeb [1]

[1]Department of Chemistry, Faculty of Science, Menoufia University, Shebin El -Kom, Egypt.
[2]Department of Chemistry, Faculty of Science, Benha University, Egypt.

Abstract

Organometallic drugs of Ca(II), Fe(III), Co(II), Ni(II), Cu(II), Zn(II), Ag(I), Cd(II), Hg(II) and Pb (II) with N-(4-aminophenyl)-2-hydroxybenzamide ligand have much potential as therapeutic and cytotoxic agents against Prostatic carcinoma cell line (PC-3). Specific examples involving the design of metal complexes as anticancer and antimicrobial agents are discussed. These complexes have been synthesized and characterized using transmission electron microscope (TEM), Scanning electron microscope with EDEX, (mass, IR, UV-VIS and ESR) spectroscopy, XRD, as well as magnetic moments, conductance, elemental and thermal analyses. Molar conductance in DMF solution indicates that, the complexes are non-electrolytes. The ESR spectra of solid Cu (II) complex **(8)** showed isotropic type indicating an octahedral geometry with covalent bond character. X-ray Diffraction Spectroscopy XRD has been done. The XRD reveal that cu(II) complex **(6)** , Zn (II) complex **(11)** and Ag (I) complex **(12)** these complexes have the average crystallite sizes of 27.1,22.6 and 7.11 nm respectively. It was suggested that the complexes were Nano crystalline. Fluorescence spectroscopy had been done for HL **(1)**, CU (II) complex **(6)**, Zn (II) complex **(11)** and Ag (I) complex **(12)**. Cytotoxic evolution against Prostatic carcinoma cell line of the ligand and its complexes have been carried out. Ligand **(1)** and its complexes showed enhanced activity in comparison to the standard drug (Cisplatin) was applied with IC_{50} = *8.51-401.18 µg/ml* range. Zn(II) complex **(11)** was the most potent cytotoxic agent against prostatic carcinoma with IC_{50} = *8.51 µg/ml which candidates as anticancer agent. Also Antimicrobial activity had been carried out.*

Keywords: Amide ligand, complexes, magnetism, ESR, XRD, cytotoxicity, prostatic carcinoma.

Introduction

The American Cancer Society estimates that there will be 248,530 new cases of prostate cancer in 2021 and more than 3.1 million prostate cancer survivors in the United States [1]. The American Cancer Society also estimates that prostate cancer will be the second leading cause of cancer-related death in US men after lung cancer in 2021 [2]. Furthermore, rates of

prostate cancer are higher in men of African descent compared with men of European descent [3]. Germ line testing (genetic testing for genes linked with hereditary cancer risk has emerged as integral to prostate cancer precision treatment in the metastatic setting, is increasingly informing screening strategies, and provides hereditary cancer information for men and their families [4]. In recent years, there has been an exponential rise in understanding the role of genetic mutations in prostate cancer predisposition and the development of new precision therapies [5, 6]. Many genes are now incorporated into the guidelines for genetic testing to assess the risk of developing prostate cancer and offer guidance for targeted therapeutics [7]. In May 2020, the US Food and Drug Administration (FDA) approved 2 poly(adenosine diphosphate [ADP]-ribose) polymerase (PARP) inhibitors for the treatment of men with metastatic, castration-resistant prostate cancer (mCRPC) based on improved clinical responses [8]. Metallo-drugs (organometallic reagents) are pharmacologically active compounds having metal atoms, which are essential for their microbial and antitumor activities, such as anticancer [9]. Metallo-drugs offer many features over purely organic compounds due to specific characteristics of coordination compounds. Their bioactivity is affected by the type of central atom, its coordination and oxidation number, type and number of the ligands, coordination geometry and charge of the complex [10]. In recent years, the coordinated Chemistry of diamines have attracted the attention of researchers due to their unique capability of constructing complicated organic molecules using centres of metal as intermediates. For example, N-phenyl-ortho-phenylenediamine coordinated to platinum or nickel atoms transforms into imidazophenazine derivatives [11]. The coexistence of hydrolizable ester group (-COO-) and amide group (-NHCO-), which are capable of establishing strong intermolecular hydrogen bond interactions, becomes fundamental to obtaining a suite of materials with tailored properties. Specifically, different polyester amides have been developed for biomedical applications such as drug delivery systems [12]. Literature survey reveals that nitrogen - and sulfur-containing compounds showed very good bioactivity, being potentially active against cancer as well as viral and fungal diseases [13]. The amide moiety has attracted further interest because it is widespread in natural and synthetic drugs and shows lower toxicity [14]. Bioactivity of amides can also be achieved by constructing the amide with hydroxypentanedioate [15]. In a variety of disciplines, such as environmental, inorganic, analytical chemistry, and bio-medical science, the fluorescence spectroscopy has developed into a common sensor that detects a highly useful substance. They have offered highly sensitive, selective, and accurate online and cost-effective detection of harmful ions of heavy metal, enzymes, and anions [16]. The purpose of the research is to prepare and spectroscopically characterized new metal complexes of amide ligand and also to develop an analytical method for quickly and economically detecting

amide ligand. The using of spectro fluorimetric approach which has excellent simplicity, sensitivity, and selectivity. Prostate cancer affects men of all racial and ethnic groups and leads to higher rates of mortality in those belonging to a lower socioeconomic status due to late detection of the disease. There is growing evidence that suggests the contribution of an individual's genetic profile to prostate cancer [17]. Currently used prostate cancer treatments have serious adverse effects; therefore, new research is focusing on alternative treatment options such as the use of genetic biomarkers for targeted gene therapy, nanotechnology for controlled targeted treatment, and further exploring medicinal plants for new anticancer agents. Herein, we reported synthesis and characterization of new metallo-therapeutic candidates derived from the novel ligand 1 N-(4-aminophenyl)-2-hydroxybenzamide ligand. The cytotoxic activity of synthesized compounds has been also investigated.

Materials and methods

All the reagents employed for the preparation of the ligand and its complexes were synthetic grade and used without further purification. TLC is used to confirm the purity of the compounds. C, H, N and Cl analyses were determined at the Analytical Unit of Cairo University, Egypt. A standard gravimetric method was used to determine metal ions [18]. All metal complexes were dried under vacuum over P_4O_{10}. The IR spectra were measured as KBr pellets using a Perkin-Elmer 683 spectrophotometer (4000-400 cm-1). Electronic spectra (qualitative) were recorded on a Perkin-Elmer 550 spectrophotometer. The conductance(10^{-3}M) of the complexes in DMF were measured at 25°C with a Bibby conduct meter type MCl. ^{1}H-NMR spectra of the ligand and its Cd(II) complex were obtained with Perkin-Elmer R32-90-MHz spectrophotometer using TMS as internal standard. Mass spectra were recorded using JEULJMS-AX-500 mass spectrometer provided with data sys-tem. SEM using Edex and transmission electron microscope (TEM) for the prepared complexes were recorded at electron microscope unit faculty of Science Alexandria University. The thermal analyses (DTA and TGA) were carried out in air on a Shimadzu DT-30 thermal analyzer from 27 to 800°C at a heating rate of 10°C per minute. Magnetic susceptibilities were measured at 25°C by the Gouy method using mercuric tetrathiocyanatocobalt(II) as the magnetic susceptibility standard. Diamagnetic corrections were estimated from Pascal's constant [19]. The magnetic moments were calculated from the equation: The ESR spectra of solid complexes at room temperature were recorded using a varian E-109 spectrophotometer; DPPH was used as a standard material. The TLC of all compounds confirmed their purity. The fluorescence spectroscopy has developed into a common sensor that detects a highly useful substance. They have offered highly sensitive, selective, and accurate online and cost-effective detection of harmful ions of heavy metal, enzymes, and anions [20]. The purpose of the research is to

prepare and spectroscopically characterized new metal complexes of amide ligand and also to develop an analytical method for quickly and economically detecting amide ligand. The Using spectrofluorimetric approach which has excellent simplicity, sensitivity, and selectivity. per minute. All fluorescence measurements were acquired by an FS5 spectrofluorometer (Edinburgh, UK) with a 150 W xenon lamp source for excitation. Also, with 1-cm quartz cell and connected to Fluoracle® software. The slit widths were set to 2 nm and scanning speed 1000 nm/min.

Experimental

HL**;(1)** was prepared as shown in scheme 1 and then was stirred for 30 minutes. After cooling, the solvent was removed under reduced pressure to give crude product which was crystallized in ethanol to yield pure ligand (**1**). Ligand (1): Yield 83 %; m.p. 296; color is Black; Anal. Calcd. (%) for C13H14N2O3 (FW = 246.26): C, 63.40; H, 5.73; N, 11.38; Found (%) C, 63.64; H, 5.64; N, 11.54; IR (KBr, cm^{-1}), 3450 υ(OH), 3123 υ(NH), 3423 υ(NH_2), 1627 υ(C=O), 1512, 760 υ(C=C)Ar.

Synthesis of metal complexes (2)-(15): The metal complexes **(2)** and **(3)** were prepared by refluxing with string a suitable amount (1 mmol) of a hot ethanolic solution of the following metal salts and ($CaCl_2.2H_2O$),($FeCl_3.3H_2O$), ($Co(CH_3COO)_2.4H_2O$), ($Ni(CH_3COO)_2.4H_2O$), ($Cu(CH_3COO)_2.H_2O$), ($CuCl_2.2H_2O$), ($CuSO_4.5H_2O$), ($Zn(CH_3COO)_2.2H_2O$), (AgNO3), ($Cd(CH_3COO)_2.2H_2O$), ($HgCl_2$), ($Pb(CH_3COO)_2.2H_2O$) to prepare complexes **(2-4),(6)** and **(12)** with molar ratio (1M:1L) respectively. On the other hand ethanolic solution of metal salts was added to Ligand solution with molar ratio (1M:2L) to afford metal complexes **(4-5), (8-11),(13)** and **(15)**. From another way solvation of metal salts with ethanol and then added the ligand solution with molar ratio (2M:1L) to obtain metal complex **(7)**.The refluxing times varied from 2 to 4 hours according to the depending to nature of metal ion. 3 mL of diethyl amine were added to the reaction mixture in order to initiate precipitation of complex. The precipitates, were filtered off, washed with ethanol then by diethyl ether and dried in vacuum desiccators over P_4O_{10}.

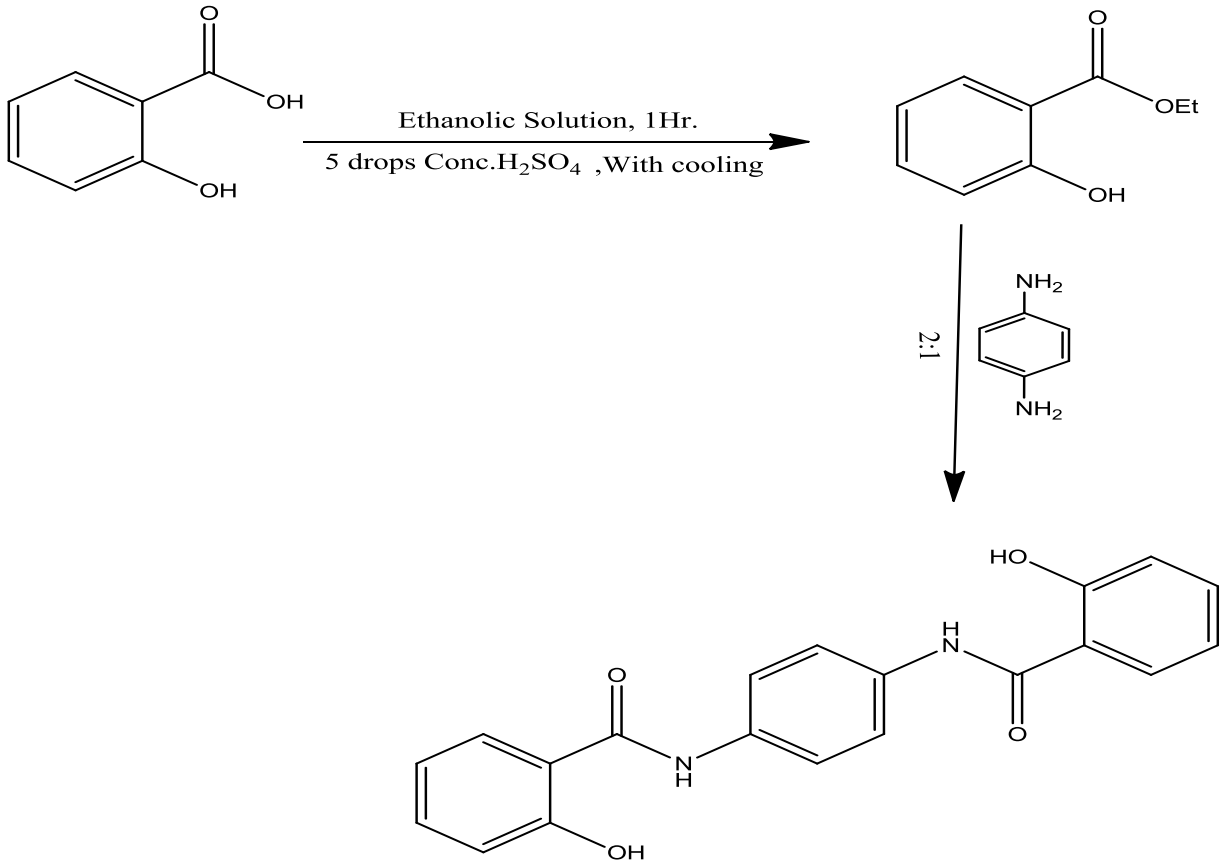

Scheme 1: Preparation of Ligand HL **(1)**

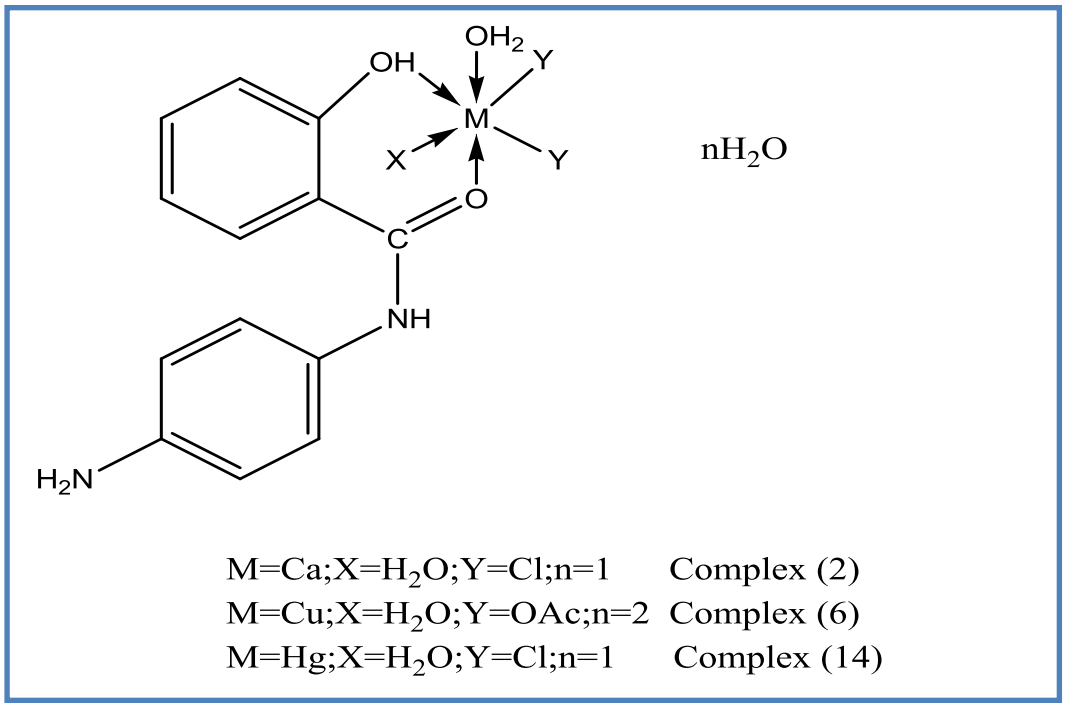

Fig (1). Chemical structure of Ca(II) complex **(2)**,Cu(II) complex **(6)** and Hg(II) complex **(14)**

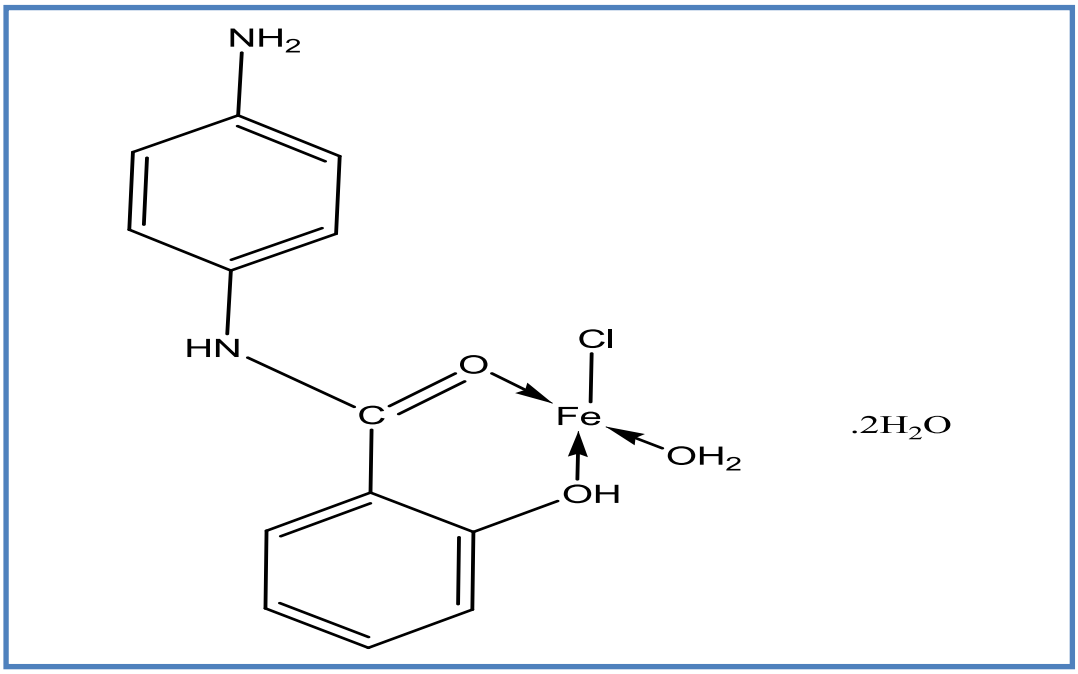

Fig (2). Chemical structure of Fe(III) Complex **(3)**

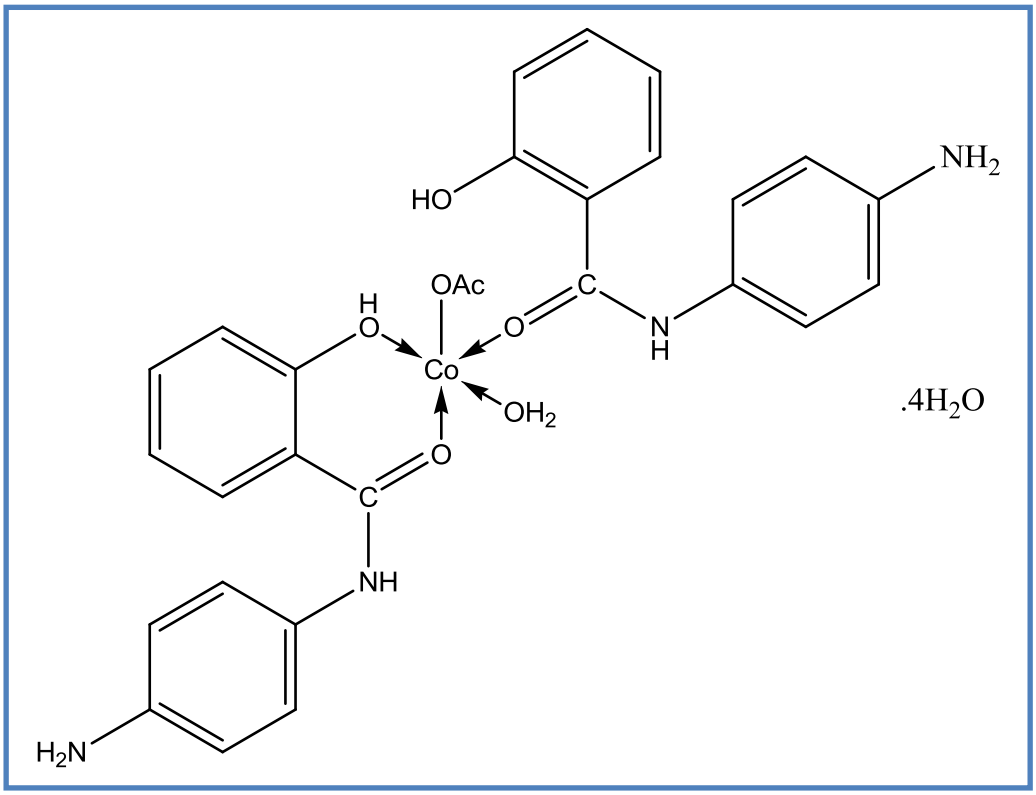

Fig (3). Chemical structure of Co (II) Complex **(4)**

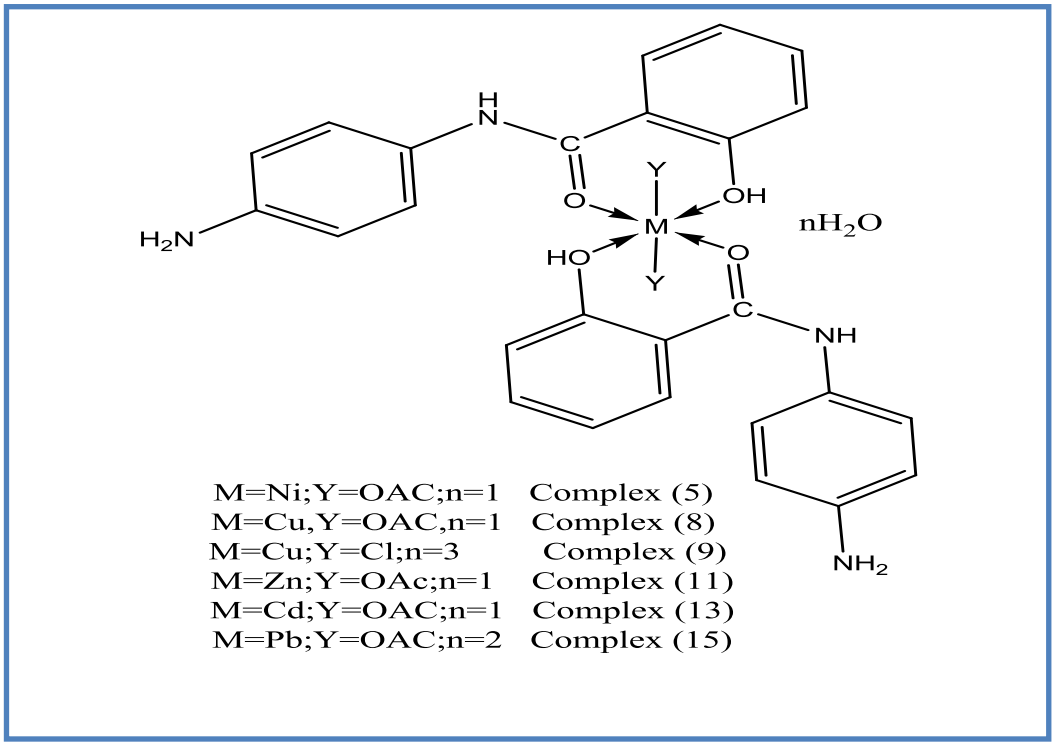

Fig (4) Chemical structure of Ni (II) complex **(5)**, Cu (II) complex **(8)**,**(9)**, Zn (II) complex **(11)**, Cd (II) complex **(13)** and Pb (II) complex **(15)**

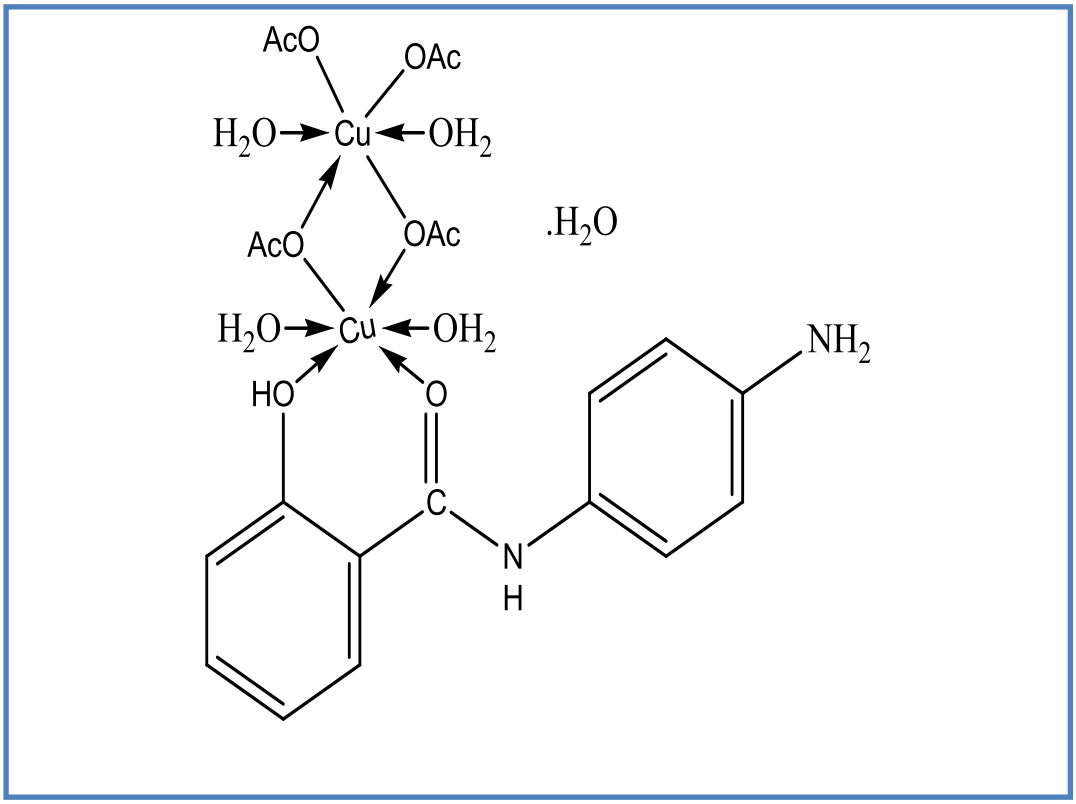

Fig (5). Chemical structure of Cu (II), complex **(7)**

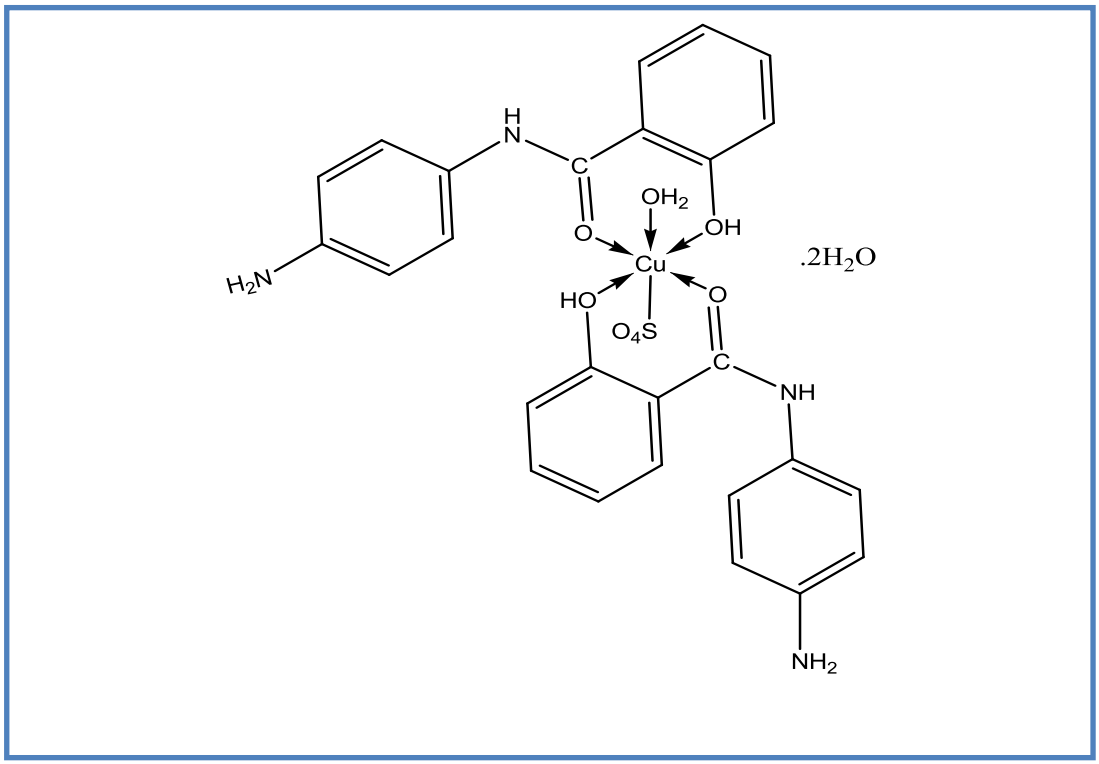

Fig (6). Chemical structure of Cu (II), complex **(10)**

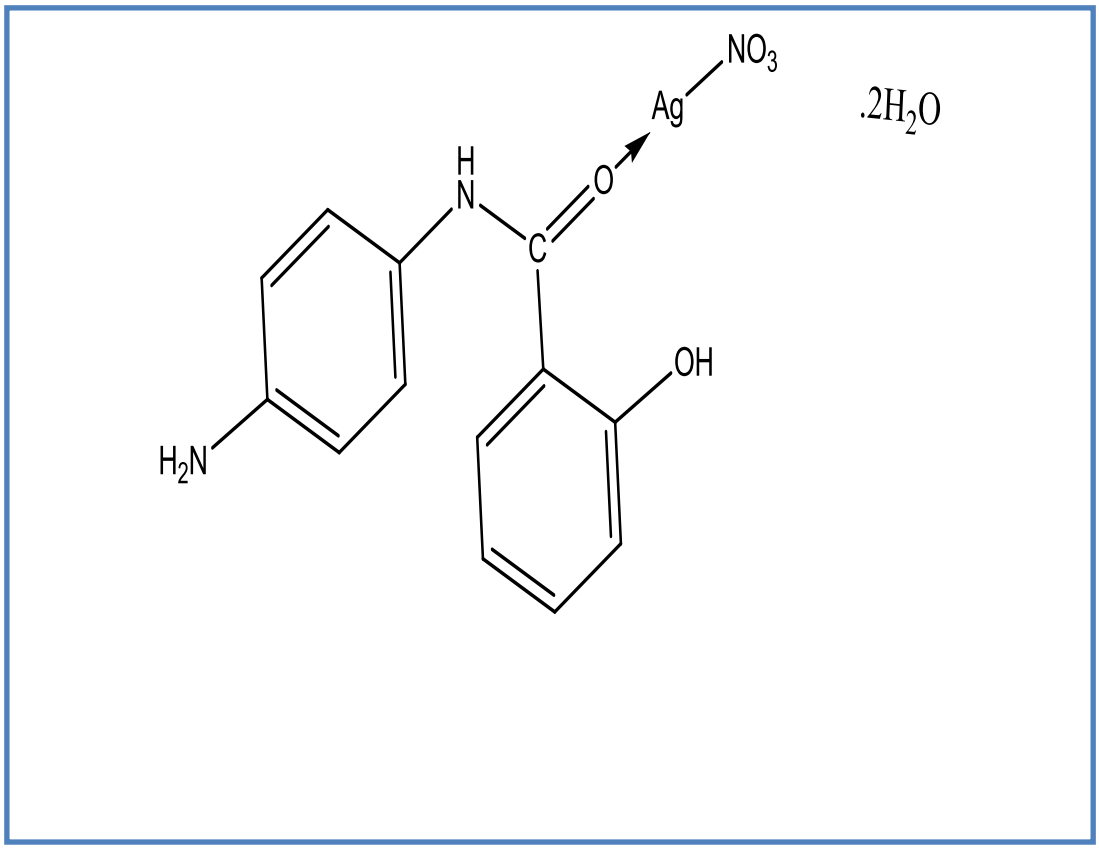

Fig (7). Chemical structure of Ag (I), complex **(12)**

Biological activity

Cytotoxic activity:

Mammalian cell lines: PC-3 (prostate carcinoma) were obtained from VACSERA Tissue Culture Unit.

Chemicals used: Dimethyl sulfoxide (DMSO), crystal violet and trypan blue dye were purchased from Sigma (St. Louis, Mo., USA).

Fetal Bovine serum, DMEM, RPMI-1640, HEPES buffer solution, L-glutamine, gentamycin and 0.25% Trypsin-EDTA were purchased from Lonza.

Crystal violet stain (1%): It composed of 0.5% (w/v) crystal violet and 50% methanol then made up to volume with ddH_2O and filtered through a Whatmann No.1 filter paper.

Cell line Propagation:

The cells were propagated in Dulbecco's modified Eagle's medium (DMEM) supplemented with 10% heat-inactivated fetal bovine serum, 1% L-glutamine, HEPES buffer and 50µg/ml gentamycin. All cells were maintained at 37ºC in a humidified atmosphere with 5% CO_2 and were subcultured two times a week.

Cytotoxicity evaluation using viability assay: For cytotoxicity assay, the cells were seeded in 96-well plate at a cell concentration of 1×10^4 cells per well in 100µl of growth medium. Fresh medium containing different concentrations of the test sample was added after 24 h of seeding. Serial two-fold dilutions of the tested chemical compound were added to confluent cell monolayers dispensed into 96-well, flat-bottomed microtiter plates (Falcon, NJ, USA) using a multichannel pipette. The microtiter plates were incubated at 37ºC in a humidified incubator with 5% CO_2 for a period of 24 h. Three wells were used for each concentration of the test sample. Control cells were incubated without test sample and with or without DMSO. The little percentage of DMSO present in the wells (maximal 0.1%) was found not to affect the experiment. After incubation of the cells for at 37°C, for 24 h, the viable cells yield was determined by a colorimetric method. In brief, after the end of the incubation period, media were aspirated and the crystal violet solution (1%) was added to each well for at least 30 minutes. The stain was removed and the plates were rinsed using tap water until all excess stain is removed. Glacial acetic acid (30%) was then added to all wells and mixed thoroughly, and then the absorbance of the plates were measured after gently shaken on Microplate reader (TECAN, Inc.), using a test wavelength of 490 nm. All results were corrected for background

absorbance detected in wells without added stain. Treated samples were compared with the cell control in the absence of the tested compounds. All experiments were carried out in triplicate. The cell cytotoxic effect of each tested compound was calculated**.** The optical density was measured with the microplate reader (SunRise, TECAN, Inc, USA) to determine the number of viable cells and the percentage of viability was calculated as [(ODt/ODc)]x100% where ODt is the mean optical density of wells treated with the tested sample and ODc is the mean optical density of untreated cells. The relation between surviving cells and drug concentration is plotted to get the survival curve of each tumor cell line after treatment with the specified compound. The 50% inhibitory concentration (IC_{50}), the concentration required to cause toxic effects in 50% of intact cells, was estimated from graphic plots of the dose response curve for each conc. using Graphpad Prism software (San Diego, CA. USA) [21].

Table (1). Analytical and physical data of ligand and its metal complexes.

No.	Ligand/Complexes	Color	FW	M.P (^{O}C)	Yield (%)	Anal. /Found (Calc.) (%)				
						C	**H**	**N**	**M**	**Conductivity Λ***
(I)	**$C_{13}H_{14}N_2O_3$ (HL)**	Gray	300.31	**140**	**94**	**64.40 (64.11)**	**5.73 (5.11)**	**11.38 (11.99)**	**-**	**-**
(2)	**$C_{13}H_{20}CaCl_2N_2O_6$ ((HL)$CaCl_2H_2O_2$).$2H_2O$**	Black	694.01	**285**	86	**37.96 (37.92)**	**4.90 (4.23)**	**6.81 (6.07)**	**9.47 (9.42)**	**9.0**
(3)	**$C_{13}H_{18}Cl_3FeN_4O_5$ ((HL)$FeCl_3H_2O$).$2H_2O$**	pale Black	509.99	**>300**	85	**35.13 (35.75)**	**4.08 (4.93)**	**6.30 (6.49)**	**12.56 (12.46)**	**9.2**
(4)	**$C_{28}H_{39}CoN_4O_{11}$ ((2HL)Co(H_2O)(OAc)] .$4H_2O$**	Black	664.55	**280**	80	**50.45 (50.61)**	**5.90 (5.61)**	**8.41 (8.43)**	**8.84 (8.87)**	**77.2**
(5)	**$C_{30}H_{32}N_4NiO_9$ ((2HL)Ni $(OAc)_2$).H_2O**	Black	778.24	**360**	82	**55.32 (55.13)**	**4.95 (4.44)**	**8.60 (8.20)**	**9.01 (9.17)**	**45.8**
(6)	**$C_{19}H_{30}CuN_2O_{10}$ ((HL)Cu $(OAc)_2(H_2O)_2$).$2H_2O$**	Dark Black	776.68	**>300**	80	**44.75 (44.29)**	**5.93 (5.28)**	**5.49 (5.21)**	**12.46 (12.99)**	**6.3**
(7)	**$C_{22}H_{38}CuN_2O_{15}$ ((HL)$Cu_2(OAc)_2(H_2O)_2$**	Black	699.04	**262**	**85**	**37.88 (37.67)**	**5.49 (5.19)**	**4.02 (4.81)**	**18.22 (18.09)**	**31.8**
(8)	**$C_{30}H_{32}CuN_4O_9$ ((2HL)Cu$(OAc)_2$).H_2O**	Black	697.63	**350**	**90**	**54.92 (54.88)**	**4.92 (4.49)**	**8.45 (8.02)**	**9.68 (9.22)**	**10.4**
(9)	**$C_{26}H_{30}Cl_2CuN_4O_7$ ((2HL)$CuCl_2$).$3H_2O$**	Black	610.26	**>300**	**90**	**48.42 (48.11)**	**4.69 (4.21)**	**8.69 (8.18)**	**9.85 (9.62)**	**1.5**
(10)	**$C_{26}H_{30}CuN_4O_{11}S$ ((2HL)Cu$(SO_4)(H_2O)$).$2H_2O$**	Black	656.14	**259.2**	**88**	**46.60 (46.92)**	**4.51 (4.92)**	**8.36 (8.54)**	**9.84 (9.68)**	**26.6**
(11)	**$C_{30}H_{32}N_4O_9Zn$ ((2HL)Zn $(OAc)_2$).H_2O**	Dark Black	795.08	**251.6**	**75**	**54.76 (54.32)**	**4.90 (4.32)**	**8.52 (8.05)**	**9.94 (9.14)**	**26.8**
(12)	**$C_{13}H_{16}AgN_3O_7$ ((HL)Ag NO_3).$2H_2O$**	Black	444.50	**255**	**80**	**35.96 (35.13)**	**3.71 (3.08)**	**9.68 (9.30)**	**24.85 (24.56)**	**11.4**
(13)	**$C_{30}H_{34}CdN_4O_{10}$ ((HL)Cd$(OAc)_2$).$2H_2O$**	Gray	433.13	**285**	**80**	**49.84 (49.96)**	**4.74 (4.91)**	**7.75 (7.68)**	**15.55 (15.85)**	**23.7**
(14)	**$C_{13}H_{18}Cl_2HgN_2O_5$ ((HL)$HgCl_2(H_2O)2$).H_2O**	Black	411.29	**340**	**85**	**28.19 (28.96)**	**3.28 (3.90)**	**5.06 (5.81)**	**56.22 (56.74)**	**3.6**

(15)	**$C_{28}H_{31}N_4O_9Pb_2$ ((2HL)Pb(OAc)(H2O)).3H_2O**	Pale Black	553.79	**310**	**80**	**34.25 (34.19)**	**3.18 (3.28)**	**5.71 (5.06)**	**42.20 (42.82)**	**5.6**

^{1}H-NMR spectra of the ligand (1) and complexes (11, 13 and 15):

The ^{1}H-NMR spectra of ligand (1) and complex (11) in deutrated DMSO showed peaks consistent with the proposed structure.The ^{1}H-NMR spectrum of the ligand showed chemical shift observed as singlet at 10.53 ppm which was assigned to proton of hydroxyl group. The chemical shift which appeared at 8.3 ppm was attributed to the proton of NH attached to (CH- of aromatic ring); (CO-NH-Ar-). However, The NH_2 proton of aromatic was observed as a singlet at 6.3 ppm. A set of signals appeared as multiples in the 6.6-6.9 ppm range, corresponding to protons of aromatic ring [22].By comparison the ^{1}HNMR of the ligand and the spectrum of the complex (11); signal was observed as a singlet at 10.4 ppm characteristic to the O*H* group indicating that the ligand found in the protonated form. In addition, there is a significant downfield shift of the NH attached to (CH- of aromatic ring); (CO-NH-Ar-) proton signal relative to the free ligand clarified that the metal ions are coordinated to the amide nitrogen atom. This shift may be due to the formation of a coordination bond (NHC═O-M)) [23] (Chart (1))

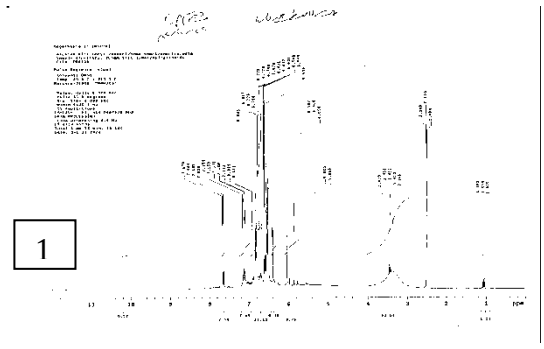

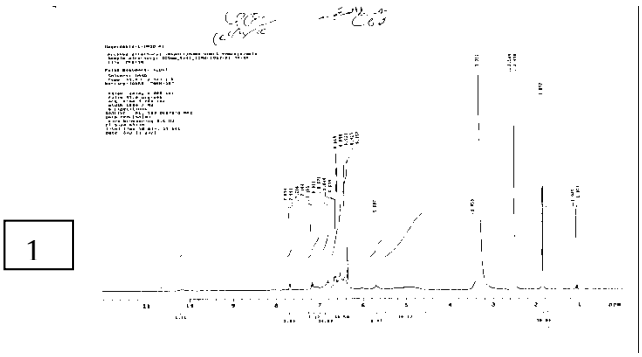

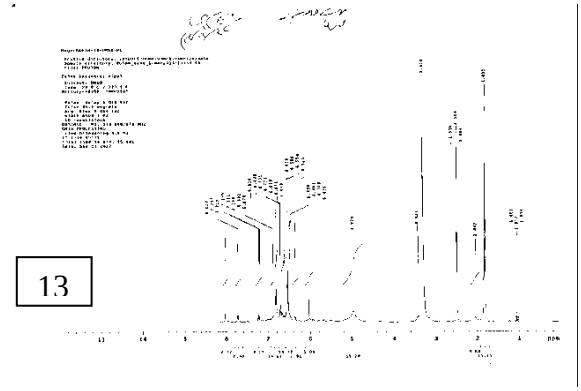

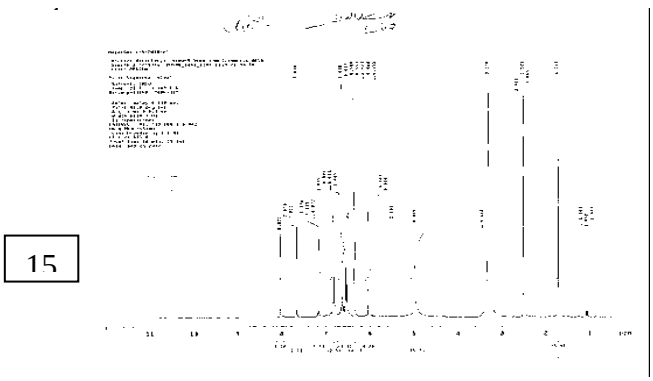

Chart (1): ^{1}H-NMR spectra of the ligand (1) and complexes (11, 13 and 15)

IR spectra:

The mode of bonding between the ligand and the metal ion revealed by comparing the IR spectra of the ligand (1) and its metal complexes (2)-(15). The ligand showed bands in the 3600-3340 and 3330-2650 cm^{-1} ranges, commensurate the presence of two types of intra- and intermolecular hydrogen bonds of OH and NH groups with carbonyl group [24]. Thus, the higher frequency band was associated with a weaker hydrogen bond. The medium band appeared at 3123 cm^{-1} was assigned to υ (NH) group [25]. The υ (NH) group in the complexes appeared nearly at the same region of the free ligand indicating that, the NH group is not involved in the coordination to the metal ion [26]. However, the characteristic bands of υ (NH_2) and υ (C═O) amide were observed at (3423 and 3390) and 1627 and cm^{-1} respectively. Strong band appeared at 3450-1215 cm^{-1} was attributed to the υ (C-OH) vibration. The bands appeared at 1512, 1460, 760 and 710 cm^{-1} range, were assigned to υ (Ar) vibration [27]. By comparing the IR spectra of the complexes (2)-(15) with that of the free ligand. It was found that, The υ (NH_2) group in the complexes appeared nearly at the same region of the free ligand indicating that, the NH_2 group is not involved in the coordination to the metal ion [28]. The υ (C═O) amide complexes appeared at 1630-1610 cm^{-1} range indicating that, the υ (C═O) amide group was involved in the coordination to the metal ion [29]. In acetate complexes, (5-8), (11),(13) and (15) in these complexes bands were observed in the 1576-1340 cm^{-1} range suggesting the coordination of acetate group in these complexes as a monodentate, fashion [30]. The sulphato complex (10) showed bands at 1178, 1115, 1021 and 652 cm^{-1} respectively assigned to monodentate sulphate group [31]. Complexes (12) show bands at 1380,1250 and 850 cm^{-1} range these have been assigned to the nitrato group. Complexes (11)-(12) show bands in the 590-535cm^{-1} was assigned to υ (M-N) [32]. Complexes (2-15) showed bands in the 668-603cm^{-1} range due to υ (M- O) [33] . Complexes (2),(3),(9) and (14) showed bands in the 482-418cm^{-1} range this has been assigned to the υ (M-Cl).

Table (2):- IR Frequencies of the bands (cm^{-1}) of the ligand [HL], (1) and its metal complexes

No.	ν(OH)	υ(H-bonding)	ν(NH)	ν(O=C-N)	ν(NH_2)	ν(C=O) Amide	ν(Ar)	ν(OAc)/SO_4 /NO_3)	υ(M-O)	υ(M-N)	υ(M-Cl)
(1)	3450,1215	3600-3340 3330-2650	3123	-	3423,3390	1627	1512,1460 760,710	-	-	-	-
(2)	3445-3402 1282,1303	3650-3340 3330-2670	3120	-	3385,3365	1618, 1612	1510,1475 ,765, 735	-	666	-	480
(3)	3445-3405 1292,1275	3630-3330 3320-2680	3117	-	3385,3345	1630, 1615	1510,1485 ,1385,1355	-	625	-	425
(4)	3427,3400 1310,1278	3570-3310 3300-2720	3195	540	3380,3350	1622, 1612	1497,760	1460,1355	615	-	-
(5)	3445,3423 1292,1245	3610-3320 3310-2650	3221	-	3386,3362	1610	1506,1415,761, 705	1568,1425	617	-	-
(6)	3470,1381 ,1281	3560-3250, 3240-2800	3190	-	3380,3350	1616	1504,763	1490,1386	616	-	-
(7)	3450,3400 1309,1280	3600-3350 3300-2780	3210	1640,162 5	3380,3350	1625	1529,770 1511,730	1576,1490 1392,1340	652,603	-	-
(8)	3470,1381, 1281	3560-3250 3240-2800	3190	-	3380,3350	1616	1504,763	1490,1386	616	-	-
(9)	3445,3426 1305,1275	3560-3240 3230-2700	3220	-	3380,3365	1622, 1615	1505,1405 763,705	-	613	-	418
(10)	3448,3425 1306,1252	3570-3320 3310-2570	3216	-	3378,3330	1635	1508,1490,760, 710	1178,1115 1021,652	618	-	-
(11)	3446,3480 1337,1277	3560,3310 3300,2750	3210	-	4450,3325	1625, 1618	1512,760	1547,1390	617	590	-
(12)	3455,3435 1302,1290	3600-3340 3300-2450	3120	-	4480.3360	1635	1505,1482 760,730	1380,1250 850	615	535	-
(13)	3445,3405 1300,1278	3620-3320 3310-2750	3217	-	3382,3365	1630, 1612	1500,1482 760,730	1492,1278	620	-	-
(14)	3446,3405 1307,1282	3650,3310 3300,2750	3120	-	3382,3355	1619, 1612	1509,1405 765,735	-	619,668	-	482
(15)	3445,3400 1279,1258	3560-3280 3270-2480	3215	-	3365,3350	1625, 1616	1585,747 1513,715	1447,1342	615	-	-

Mass spectra

The mass spectra of (1) and its, Ca(II) complex (2) Ag(I) complex (12) and Hg(II) complex (14) confirmed their proposed formulation. The spectrum of (1) reveals the molecular ion peak (m/z) at 246 amu consistent with the molecular weight of the ligand. Furthermore, the fragments observed at (m /z) = 49,08, 79.90, 137, 146.20,182.49,233.02and246.40amu correspond to C_2 H_4,C_5H_3O, $C_7H_7NO_2$, $C_9H_{10}NO_2$, $C_9H_{12}NO_3$, $C_{12}H_{13}N_2O_3$ and, $C_{13}H_{14}N_2O_3$ moieties respectively. Complex (2) shows fragments (m/z) at 64.43, 117.80, 147.35, 191.94, 266.47, 311.53and 375.65amu due to C_5H_3, C_8H_4O, $C_9H_6O_2$, $C_9H_{10}CaO_2$, $C_{11}H_{12}CaClNO_2$, $C_{12}H_{15}CaClN_2O_3$ and $C_{13}H_{16}CaCl_2N_2O_4$

moieties respectively. The fragments observed (m⁄z) at 77.23,90.12,178.23,329.09,406.31and 435.29 amu for complex (12) were assigned to C_3H_6,C_7H_7, $C_9H_6NO_3$, $C_{10}H_6AgNO_5$, $C_{11}H_{11}AgN_3O_7$, and $C_{13}H_{16}AgN_3O_7$ moieties, whereas the spectrum of Hg(II) complex (14) showed molecular ion peak at 554.15 assigned to the molecular weight of the complex and also showed fragments at 76.75, 175.33, 408.26, 438.39, 460.20, 448,524.41and554.15 which were assigned to C_6H_3, $C_{10}H_3ClO$, $C_{10}H_3ClHgO_3$, $C_{11}H_5ClHgO_4$, $C_{11}H_{13}ClH_9NO_4$, $C_{12}H_{14}Cl_2HgNO_5$ and $C_{13}H_{18}Cl_2HgN_2O_5$. moieties respectively.

Magnetic moments:

The magnetic moments of the metal complexes (4-13) and (15) at room temperatures were shown in (Table 1). Co (II) complex (4) showed value in the 4.75B.M, range corresponding to one unpaired electron in an octahedral structure [34]. Ni (II) complex (**5**) showed value in the 3.12 B.M, range corresponding to one unpaired electron in an octahedral structure, Cu (II) complexes (6-10) showed values in the1.17, 1.65,1.69and1.70B.M, range corresponding to one unpaired electron in an octahedral structure. Zn (II) complex (11), Ag (I) complex (12), Cd (II) complex (13) and Pb (II) complex (15) showed diamagnetic property [35].

Electronic spectra:

The electronic spectral data for the ligand (1) and its metal complexes in DMF solution are summarized in (Table 3). Ligand (1) in DMF solution shows two bands at 320 nm (ε =7.72 x 10^{-3} mol^{-1} cm^{-1}) and 295 nm (ε = 7.12x 10^{-3} mol^{-1} cm^{-1}) which may be assigned to n→π* and π→π* transitions of the immine and aromatic ring respectively. Copper(II) complexes (6)-(10) show bands in the 295-275 and 310-305 nm ranges , these bands are due to intraligand transitions, however, the bands appear in the 495-455, 580-500 and 620-600 nm ranges, are assigned to O→Cu, charge transfer, $^2B^1 \rightarrow {}^2E$ and $^2B1 \rightarrow {}^2B2$ transitions, indicating a distorted tetragonal octahedral structure. However, cobalt(II) complex (4) shows bands at 285,300,400,440,510,585,620 and 623 nm, the first two bands are within the ligand and the other bands are assigned to $^4T1g(F) \rightarrow {}^4T2g(P)(v3)$, $^4T1g(F) \rightarrow {}^4A2g(v2)$ and $^4T1g(F)$ $^4T2g(F)(v1)$ transitions respectively. Zinc (II) complexes (11) shows bands due to intra ligand transitions. However, nickel(II) complexes (**5**) shows bands at 280,295,305,307,450,656,620 and 765 nm, the first three bands are within the ligand and the other bands are attributable to O→Ni charge transfer, $^3A2g(F) \rightarrow {}^3T1g(P)(\nu 3)$, $^3A2g(F) \rightarrow {}^3T1g(F)(\nu 2)$ and $^3A2g(F) \rightarrow {}^3T2g(F)(\nu 1)$ transitions respectively, indicating an octahedral Ni(II) geometry. The ν2/ν1 ratio for (**5**) is 1.23 which are less than the usual range of 1.5-1.75, indicating a distorted octahedral Ni (II) complex [36].

Table (3). The electronic absorption spectral bands (nm) and magnetic moments (B.M) for the ligands (1),(2) and their metal complexes.

No.	Ligand/Complexes	λ_{max} (nm)	μ_{eff} (BM)	ν_2/ν_1
(1)	[HL]	295 nm (ε = 7.12x 10^{-3} mol^{-1} cm^{-1}) 320 nm (ε= 7.72 x 10^{-3} mol^{-1} cm^{-1})	-	-
(4)	((2HL)Co(H_2O)(OAc)] .4H_2O	285,300 ,585,620	4.75	-
(5)	((2HL)Ni ($OAc)_2$).H_2O	280,295,305 ,620,765	3.12	-
(6)	((HL)Cu ($OAc)_2$(H_2O)2).2H_2O	290,310,540,600	1.70	-
(7)	((HL)Cu_2($OAc)_2$(H_2O)2	295,560,615	1.65	-
(8)	((2HL)Cu($OAc)_2$).H_2O	290,310,600	1.70	--
(9)	((2HL)$CuCl_2$).3H_2O	285,293 ,310, 610	1.69	-
(10)	((2HL)Cu(SO_4)(H_2O)).2H_2O	275,305 ,620	1.17	-
(11)	((2HL)Zn ($OAc)_2$).H_2O	290,300,615	Dia.	-
(12)	((HL)Ag NO_3).2H_2O	285,330,420,620	Dia	-
(13)	((HL)Cd($OAc)_2$).2H_2O	385,310,300	Dia.	-
(15)	((2HL)Pb(OAc)(H_2O)).3H_2O	384,310,300	Dia.	-

Thermal analysis (DTA and TGA):

Since the IR spectra indicated the presence of water molecules, thermal analyses (DTA and TGA) were carried out to certain their nature [37]. The thermal curves in the temperature 27-800°C range for complexes (2),(3),(5),(6),(8),(9),(11),(12),(13),(14) and (15) were thermally stable up to 45 °C. Broken of hydrogen bondings occured as endothermic peak within the temperature 45-50 °C range as shown in (Table 3). Dehydration was characterized by endothermic peaks observed within the temperature 65-80°C range, corresponding to the loss of hydrated water molecules as in complexes (2),(3),(5),(6),(8),(9),(11-15) The elimination of coordinated water molecules occured in the 140-145°C range accompanied by endothermic peaks [38]. The TGA and DTA thermogram of Ca(II) complex (2) showed that,

the complex decomposed in six steps. The first occurred at 45°C with no weight loss as endothermic peak, was due to break of hydrogen bondings. The second step occur at 75°C with 8.41 % weight loss (Calc. 8.61%) as endothermic peak which could be due to the elimination of hydrated water molecule. The decomposition step which occurred at 145°C with 8.19 % weight loss(Calc. 8.61%) could be due to the elimination of two coordinated H_2O molecules. The TGA curve displayed another thermal decomposition at 265-280°C range with 16.91% weight loss (Calc. 17.07%), which could be due to the loss of coordinated chloride group. The complex showed an exothermic peak observed at 301°C was due its melting point. Finally, exothermic peaks appeared at 445, 490, 570 and 610 °C corresponding to oxidative thermal decomposition which proceeded slowly with leaving CaO with 13.74% weight loss (Calc. 13.65%) [39]. The TGA and DTA thermogram of Fe(III) complex (**3**) showed endothermic peak observed at 70 with 7.96% weight loss (Calc. 8.13%) which could be due to the elimination of hydrated water molecule. The decomposition process which occurred at 143°C with 4.31% weight loss (Calc. 4.06%) could be due to the elimination of coordinated H2O molecule. The endothermic peak observed at 270°C with 16.96% weight loss (Calc. 16.01%), could be due to the elimination of two chloride groups. Another endothermic peak observed at 309°C with no weight loss may be due to its melting point. Finally, the complex showed exothermic peaks observed at 470, 510, 580 and 600°C with 35.99% weight loss (Calc. 36.08%) corresponding to oxidative thermal decomposition which proceeded slowly with final residue, assigned to Fe_2O_3 . The TGA and DTA thermogram of Ni(II) complex (**5**) showed endothermic peak observed at 48°C, was due to break of hydrogen bondings. Another endothermic peak appeared at 65°C, with 3.12% weight loss (Calc.2.77 %), was due to loss of one hydrated water molecule. The endothermic peak observed at 140°C with 18.31% weight loss (Calc. 18.15%), could be due to the elimination of two coordinated acetate groups. Another exothermic peak observed at 302 with no weight loss may be due to its Melting point. Finally oxidative thermal decomposition occured at 425, 485, 530 and 605°C with exothermic peaks, leaving NiO with 11.41% weight loss (Calc. 11.37%) [40]. The TGA and DTA thermogram of Cu (II) complex (**6**) decomposed in five steps. The first occurred at 50°C with no weight loss as endothermic peak, was due to break of hydrogen bondings. The second step occured at 75°C with 7.91 % weight loss (Calc. 7.07%) as endothermic peak which could be due to the elimination of two hydrated water molecule. Another endothermic peak observed at 142°C with 6.88% weight loss (Calc. 7.07%) was assigned to the loss of two coordinated water molecule.. At 312°C, endothermic peak appeared which was due to melting point. Oxidative thermal decomposition occured at 475,530,595 and 610 °C with exothermic peaks, leaving CuO with 11.98% weight loss (Calc. 12.36%) [41]. The TGA and DTA thermo gram of Cu (II) complex (**8**) decomposed in five

steps. The first occurred at 45°C with no weight loss as endothermic peak, may be due to break of hydrogen bonding. The second step occurred at 70°C with 2.72% weight loss (Calc. 2.74%) as endothermic peak which could be due to the elimination of one hydrated water molecules. Another endothermic peak observed at 265,270°C with 17.36% weight loss (Calc. 18.00%) was assigned to the loss of two Acetate groups. Another endothermic peak observed at with 315°C with no weight loss was due to melting point. Oxidative thermal decomposition occured at 425,490,540 and 600 °C with exothermic peaks, leaving CuO with 11.91% weight loss (Calc. 12.04%) [42]. The TGA and DTA thermogram of Cu(II) complex (**9**) decomposed in five steps. The first occurred at 49°C with no weight loss as endothermic peak, may be due to break of hydrogen bondings. The second step occured at 80°C with 8.18% weight loss (Calc. 8.41%) as endothermic peak which could be due to the elimination of two hydrated water molecule. Another endothermic peak observed at 140°C with 11.81% weight loss (Calc. 11.02%) was assigned to the loss of two chloride groups.. At 325°C, endothermic peak appeared which was due to melting point. Oxidative thermal decomposition occured at 440,495,540, 605 and, 640 °C with exothermic peaks, leaving CuO with 12.91% weight loss (Calc. 12.27%) [43]. The TGA and DTA thermogram of Zn(II) complex (**11**) showed endothermic peak at 48°C, due to break of hydrogen bonding. Another endothermic peak observed at 65°C with 2.33% weight loss (Calc. 2.74%) as endothermic peak which could be due to the elimination of hydrated water molecule. Another endothermic peak appeared at 285,300°C, with 20.12% weight loss (Calc. 20.88%), was due to loss of two acetate groups. Another endothermic peak observed at 333°C with no weight loss may be due to its melting point. Finally oxidative thermal decomposition occured in the 425, 490, 515 and 580 and °C with exothermic peaks, leaving ZnO with 12.80% weight loss (Calc. 12.11%) [44]. The TGA and DTA thermogram of Ag(I) complex (**12**) showed endothermic peak at 48°C, due to break of hydrogen bondings. Another endothermic peak observed at 70°C with 8.81% weight loss (Calc. 8.31%) as endothermic peak which could be due to the elimination of two hydrated water molecule. Another endothermic peak appeared at 285, 300°C, with 14.59% weight loss (Calc. 14.31%), was due to loss of nitrate group. Another endothermic peak observed at 320°C with no with no weight loss may be due to its melting point. Finally oxidative thermal decomposition occured in the 350, 400, 455 and 580 and °C with exothermic peaks, leaving AgO with 28.54% weight loss (Calc. 28.38%) [45]. The TGA and DTA thermo gram of Cd(II) complex (**13**) showed that, the complex decomposed in six steps. The first occurred at 45°C with no weight loss as endothermic peak, may be due to break of hydrogen bonding. The second step occured at 70°C with 4.07 % weight loss (Calc. 4.97%) as endothermic peak which could be due to the elimination of two hydrated water molecules. The decomposition step which occurred at 150°C with 16.99% weight loss (Calc. 16.29%) could be due to the

elimination of two acetate groups. The complex showed an endothermic peak observed at 315°C was due its melting point. Finally, exothermic peaks appeared at 425, 480, 540 and 580 °C respectively corresponding to oxidative thermal decomposition which proceeded slowly with leaving CdO with 34.16% weight loss (Calc. 34.34%) . The TGA and DTA thermogram of Hg(II) complex (**14**) decomposed in six steps. The first occurred at 49°C with no weight loss as endothermic peak, may be due to break of hydrogen bondings. The second step occured at 80°C with 3.63% weight loss (Calc. 3.25%) as endothermic peak which could be due to the elimination of one hydrated water molecule. Another endothermic peak observed at 144°C with 6.36% weight loss (Calc. 6.50%) was assigned to the loss of two coordinated water groups.. At 325°C, endothermic peak appeared which was due to melting point. Oxidative thermal decomposition occured at 440,495,540, and 605, °C with exothermic peaks, leaving HgO with 35.89% weight loss (Calc. 36.45%) . The TGA and DTA thermogram of Pb(II) complex (**15**) decomposed in five steps. The first occurred at 49°C with no weight loss as endothermic peak, may be due to break of hydrogen bondings. The second step occured at 80°C with 4.22% weight loss (Calc. 4.74%) as endothermic peak which could be due to the elimination of two hydrated water molecule. Another endothermic peak observed at 270,285°C with 15.1% weight loss (Calc. 15.54%) was assigned to the loss of two acetate groups.. At 325°C, endothermic peak appeared which was due to melting point. Oxidative thermal decomposition occurred at 440,490,560, and 605, °C with exothermic peaks, leaving PbO with 29.31% weight loss (Calc. 29.40%).

Table (4). Thermal analysis data for some metal (II) complexes

Compound No. Molecular formula	Temp. (^oC)	DTA (peak)		TGA (Wt.loss %)		Assignments
		Endo	Exo	Calc	Found	
Complex (2) $((HL)CaCl_2H_2O_2).2H_2O$	45	endo	-	-	-	Broken of H-bondings
	75	endo	-	8.61	8.41	Loss of $2H_2O$ hydrated water molecules
	145	endo	-	8.61	8.19	Loss of $2H_2O$ coordinated water molecules
	265,280	endo	-	17.07	16.91	Loss of 2Cl groups
	301	endo	-	-	-	Melting point
	445,490,570,610	-	Exo	13.65	13.74	Decomposition process with the formation of CaO
Complex (3) $((HL)FeCl_3H_2O).2H_2O$	46	endo	-	-	-	Broken of H-bondings
	70	endo	-	8.13	7.96	Loss of $2H_2O$ hydrated, water molecules
	143	endo	-	4.06	4.31	Loss of H_2O coordinated, water molecules
	270			16.01	16.96	Loss of coordinated 2Cl groups
	309	endo	-	-	-	Melting point
	470,510,580,600	-	Exo	36.08	35.99	Decomposition process with the formation of Fe_2O_3
Complex (5) $((2HL)Ni(OAc)_2).H_2O$	48	endo	-	-	-	Broken of H-bondings
	65	endo	-	2.77	3.12	Loss of H_2O hydrated water molecule
	140	endo	-	18.15	18.31	Loss of coordinated 2OAc groups
	302	endo	-	-	-	Melting point
	425,485,530,605	-	Exo	11.37	11.41	Decomposition process with the formation of NiO
Complex(6) $(HLCu(OAc)_2(H_2O)_2).2H_2O$	50	endo	-	-	-	Broken of H-bondings
	75	endo	-	7.07	7.91	Loss of $2H_2O$ hydrated water molecules
	142	endo	-	7.07	6.88	Loss of $2H_2O$ coordinated water molecules
	312	endo	-	-	-	Melting point
	475,530,595,610	-	Exo	12.36	11.98	Decomposition process with the formation of Cuo
Complex(8) $((2HL)Cu(OAc)_2).H_2O$	45	endo	-	-	-	Broken of H-bondings
	70	endo	-	2.74	2.72	Loss of H_2O hydrated water molecules
	265,270	endo	-	18.00	17.36	Loss of coordinated 2 OAc groups

	315	endo	-	-	-	Melting point
	425,490,540,600	-	Exo	12.04	11.91	Decomposition process with the formation of CuO
Complex(9) $((2HL)CuCl_2).3H_2O$	49	endo	-	-	-	Broken of H-bondings
	80	endo	-	8.41	8.18	Loss of $3H_2O$ hydrated water molecules
	140	endo	-	11.02	11.81	Loss of 2 Cl groups
	325	endo	-	-	-	Melting point
	440,495,540,605	-	Exo	12.27	12.91	Decomposition process with the formation of CuO
Complex(11) $((2HL)Zn\ (OAc)_2).H_2O$	48	endo	-	-	-	Broken of H-bondings
	65	endo	-	2.74	2.332	Loss of H_2O hydrated water molecules
	285,300	endo	-	20.88	20.12	Loss of 2OAc groups
	333	endo	-	-	-	Melting point
	425,490,515,580	-	Exo	12.11	12.80	Decomposition process with the formation of ZnO
Complex(12) $((2HL)Ag\ NO_3).2H_2O$	48	endo	-	-	-	Broken of H-bondings
	65	endo	-	8.31	8.81	Loss of $2H_2O$ hydrated water molecules
	285,300	endo	-	14.31	14.59	Loss of NO_3 group
	320	endo	-	-	-	Melting point
	350,400,455,580	-	Exo	28.38	28.54	Decomposition process with the formation of AgO
Complex(13) $((2HL)Cd(OAc)_2).2H_2O$	45	endo	-	-	-	Broken of H-bondings
	70	endo	-	4.97	4.07	Loss of $2H_2O$ hydrated water molecules
	150	endo	-	16.29	16.99	Loss of 2OAc coordinated water molecules
	315	endo	-	-	-	Melting point
	425, 480, 540,580	-	Exo	34.34	34.16	Decomposition process with the formation of CdO
Complex(14) $((2HL)HgCl_2(H_2O)2).H_2O$	49	endo	-	-	-	Broken of H-bondings
	80	endo	-	3.25	3.63	Loss of H_2O hydrated water molecule
	144	endo	-	6.50	6.36	Loss of coordinated $2H_2O$groups
	325	endo	-	-	-	Melting point
	440,495,540,605	-	Exo	36.45	35.89	Decomposition process with the formation of HgO
Complex(15) $((2HL)Pb(OAc)(H2O)).3H_2O$	49	endo	-	-	-	Broken of H-bondings
	80	endo	-	4.74	4.22	Loss of $2H_2O$hydrated water molecules
	270,285	endo	-	15.54	15.1	Loss of 2 OAc groups
	325	endo	-	-	-	Melting point
	440,490,560,605	-	Exo	29.40	29.31	Decomposition process with the formation of PbO

Electron spin resonance (ESR): The ESR spectral data for complexes **(4-8)** are presented in (Table 3). The spectra of Cu(II) complexes (**6-8**) are characteristic of species d^9 configuration having axial type of a $d(x_2-y_2)$ ground state which is the most common for copper(II) complexes [46]. The complexes showed $g_{\|}>g_{\perp}>2.0023$, indicating octahedral geometry around copper (II) ion [47]. The g-values are related by the expression $G = (g_{\|}-2)/(g_{\perp}-2)$[48], where (G) exchange coupling interaction parameter (G). If G<4.0, a significant exchange coupling is present, whereas if G value > 4.0, local tetragonal axes are aligned parallel or only slightly misaligned. Complexes (**3**), (**4**) and (**5**) showed 3.14, 3.50 and 3.80 values indicating spin-exchange interactions took place between copper (II) ions. This phenomena is further confirmed by the magnetic moments values (1.43 and 1.69 B.M.). On the other hand, the $g_{\|}/A_{\|}$ value is also considered as a diagnostic term for stereochemistry [49]. The $g_{\|}/A_{\|}$ values for the copper complexes are 170.77, 170.00 and 168.5 cm^{-1} which lie just within the range expected for the tetragonal distorted octahedral copper(II)complexes (Table2). The g-value of the Cu(II) complexes with a ^2B1g ground state ($g_{\|}>g_{\perp}$) may be expressed by[50].

$$g_{\|} = 2.002 - (8K^2{}_{\|}\lambda^{\circ}/\Delta Exy) \quad (1)$$

$$g_{\perp} = 2.002 - (2K^2{}_{\perp}\lambda^{\circ}/\Delta Exz) \quad (2)$$

Where k|| and k⊥ are the parallel and perpendicular components respectively of the orbital reduction factor (K), λ° is the spin-orbit coupling constant for the free copper, ΔExy and ΔExz are the electron transition energies of $^2B1g \rightarrow {}^2B2g$ and $^2B1g \rightarrow {}^2Eg$. From the above relations, the orbital reduction factors

($K_{\|}$, K⊥, K), which are measure terms for covalence [51], can be calculated. For an ionic environment, K=1; while for a covalent environment, K<1. The lower the value of K, the greater is the covalency.

$$K^2\perp = (g\perp - 2.002)\ \Delta Exz\ /2\lambda^o \quad (3)$$

$$K^2_{\|} = (g\| - 2.002)\ \Delta Exy\ /8\lambda^o \quad (4)$$

$$K^2 = (K2_{\|} + 2K^2\perp)/3 \quad (5)$$

K values (Table 4), for the copper (II) complexes (**6**), (**7**) and (**8**) are indicating covalent bond character [52]. Kivelson and Neiman noted that, for ionic environment $g_{\|} \geq 2.3$ and for a covalent environment $g_{\|} < 2.3$ [53]. Theoretical work by Smith seems to confirm this view. The g-values reported here (Table 4) showed considerable covalent bond character. Also, the in-plane σ-covalence parameter, α^2 (Cu) was calculated by

$$\alpha^2\ (Cu) = (A_{\|}/0.036) + (g_{\|} - 2.002) + 3/7(g - 2.002) + 0.04 \quad (6)$$

The calculated values (Table 4) suggested a covalent bonding [53]. The in-plane and out of-plane π-bonding coefficients $\beta 1^2$ and β^2 respectively, are dependent upon the values of ΔExy and ΔExz in the following equations [54].

$$\alpha^2\beta^2 = (g\perp - 2.002)\ \Delta\ Exy/2\lambda o \quad (7)$$

$$\alpha^2\beta 1^2 = (g_{\|} - 2.002)\ \Delta\ Exz/8\lambda o \quad (8)$$

In this work, the complexes (**6**), (**7**) and (**8**) showed $\beta 1^2$ values 2.84, 2.71 and 2.41 indicating a moderate degree of covalence in the in-plane π-bonding [55]. β^2 value for complexes (**6**), (**7**) and (**8**) showed 2.76, 2.54 and 2.23 indicating ionic character of the out-of-plane, [55]. It is possible to calculate approximate orbital populations for d orbitals [56] by

$$A_{\|} = A_{iso} - 2B[1 \pm (7/4)\ \Delta g_{\|}] \quad \Delta g_{\|} = g_{\|} - ge \quad (9)$$

$$\alpha p,\ d^{\ 2} = 2B/\ 2B^\circ \quad (10)$$

Where A° and 2B° is the calculated dipolar coupling for unit occupancy of d orbital respectively. When the data were analyzed, the components of the [57]. Cu hyperfine coupling were considered with all the sign combinations. The only physically meaningful results are found when $A_{\|}$ and $A_\perp$ were negative. The resulting isotropic coupling constant was negative and the parallel component of the dipolar coupling 2B are negative (-196.4, -183.03 and -156.00 G). These results can only occur for an orbital involving the dx2-y2 atomic orbital on copper. The value for 2B is quite normal for copper (Il) complexes [58]. Complexes (**4**) and (**5**) showed isotropic spectra with g_{iso}= 2.03 and 2.02.

Table 5:-ESR data for some metal (II) complexes:-

No.	$g_{\parallel}$	$g_{\perp}$	g_{iso} [a]	$A_{\parallel}$ (G)	$A_{\perp}$ (G)	A_{iso} [b] (G)	G [c]	ΔE_{xy}	ΔE_{xz}	$K_{\perp}^2$	$K_{\parallel}^2$	K	K^2	$g_{\parallel}/A_{\parallel}$	α^2	$ß^2$	$ß_1^2$	-2 ß	a_d^2 (%)
(4)	-	-	2.03	-	-	-	-	-	-	-	-	-	-	-	-	-	-	-	-
(5)	-	-	2.02	-	-	-	-	-	-	-	-	-	-	-	-	-	-	-	-
(6)	2.2	2.06	2.11	95	5	35	3.33	17391	21505	0.75	0.52	0.91	0.84	200	0.61	1.23	0.85	206.3	87.8
(7)	2.17	2.05	2.13	115	10	45	3.4	17699	21277	0.61	0.45	0.74	0.56	217	0.51	1.19	0.88	228.5	97.2
(8)	2.19	2.08	2.12	120	15	50	2.38	17482	20920	0.98	0.5	0.90	0.82	156.4	0.65	1.51	0.77	131	56

a) $g_{iso} = (2g_{\perp} + g_{\parallel})/3$, **b)** $A_{iso} = (2A_{\perp} + A_{\parallel})/3$, **c)** $G = (g_{\parallel} - 2)/(g_{\perp} - 2)$

X-ray Diffraction Spectroscopy XRD pattern:

Powder X-ray Diffraction Spectroscopy XRD pattern of the Cu (II) complex **(6)**, Zn(II) complex **(11)** and Ag(I) complex **(12)** bearing CH3COO− were recorded in the range (2θ = 0–80) is shown in (Figure 8). The pattern of the metal complexes was studied to further obtain evidence about the structure of the metal complexes at wavelength 1.5406 ´Å. The XRD pattern of the Cu(II) complexes shows well defined crystalline peaks indicating that the Cu(II) ,Zn(II) and Ag(I)-Schiff base complexes were in crystalline phase. The average crystallite size of the complexes dXRD was estimated from XRD patterns by Scherer's formula: $d_{XRD} = 0.9\lambda/\beta\ (\cos\theta)$ where 'λ' is the wavelength, 'β' is the full width at half maxima and 'θ' is the diffraction angle. The XRD reveal that $[(HL)Cu(OAc)_2.(H_2O)_2].2H_2O$, $[(HL)_2Zn(OAc)_2].\ H_2O$ and $[(HL)AgNO_3].2\ H_2O$ complexes have the average crystallite sizes of 27.10, 22.60 and 7.11 nm respectively. It suggests the complexes are nanocrystalline [59].

X-ray Diffraction Spectroscopy (XRD)

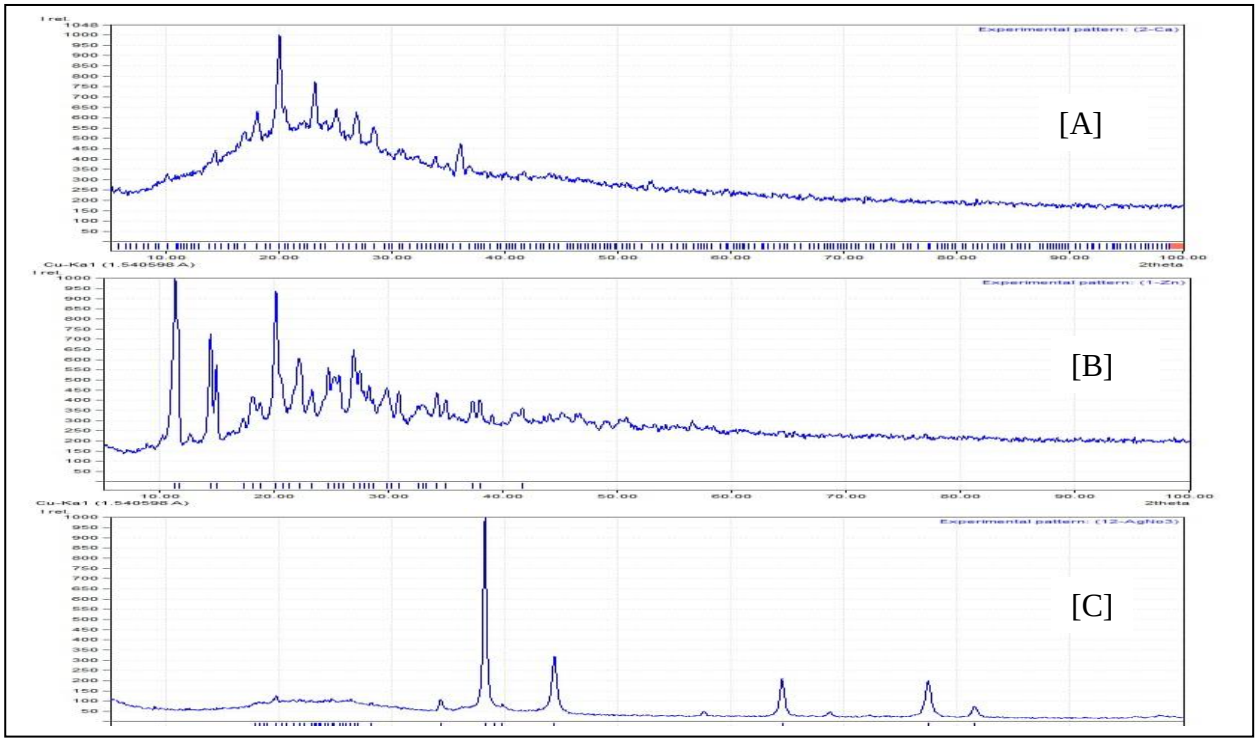

Fig. 8: X-ray Diffraction Spectroscopy XRD pattern of the Cu(II) complex (6):[A], Zn(II) complex (11):[B]

Scanning and transmission electron microscopy (SEM and TEM):

The SEM images revealed that the surface of compounds are uniformly covered by the Ligand (1) and Zn (II) complex (11) . The layers were amorphous and crystaline structures appeared. The dimention of these crystalites ranged from 7.41 to 16.71 μm Fig.4 [60].

The TEM images reveal that the average diameter of particles size of the ligand (1) and Zn (II) complex (11) were determined to be 18.53-43.75 nm and 18.31-32.77 nm respectively. Ligand and Zn (II) complex (11) were present in Nano size particle i.e., their particles present in a diameter between 1 and 100 nm in size. Ligand and complex (11) show sign with ratio that exhibit new or enhanced size-dependent properties compared with larger particles of the same material with many advantages such as: Increased bioavailability, dose proportionality, decreased toxicity, smaller dosage form (i.e., smaller tablet), stable dosage forms of drugs which are either unstable or have unacceptably low bioavailability in non-Nano particulate dosage forms, increased active agent surface area results in a faster dissolution of the active agent in an aqueous environment, such as the human body, faster dissolution generally equates with greater

bioavailability, smaller drug doses, less toxicity and reduction in fed/fasted variability [61].

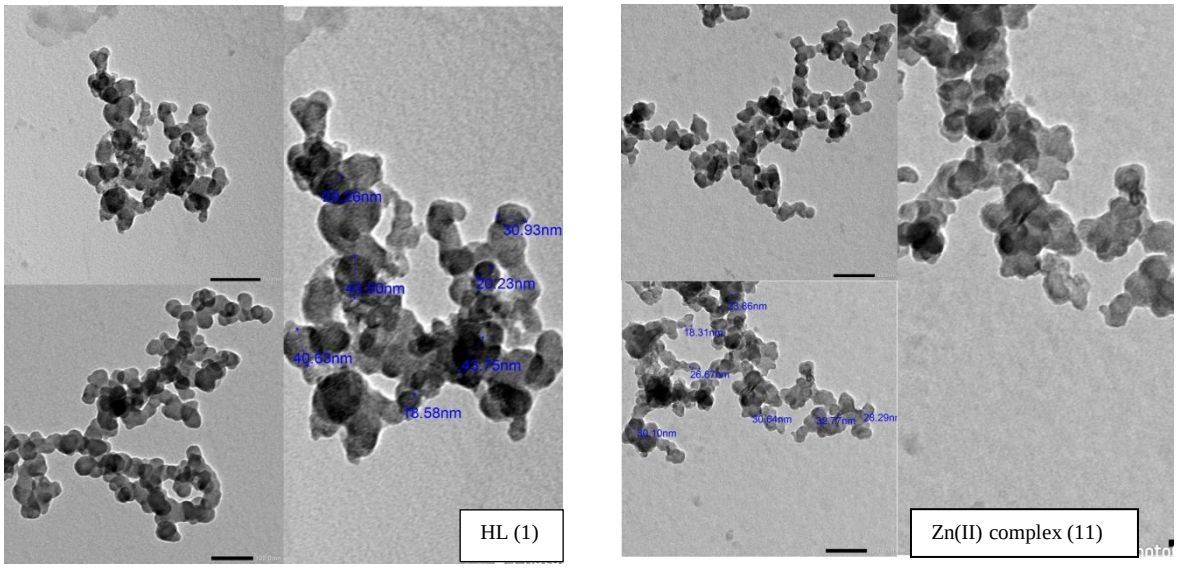

Fig. 9. TEM images for HL (1) and ZN(II) Complex (11)

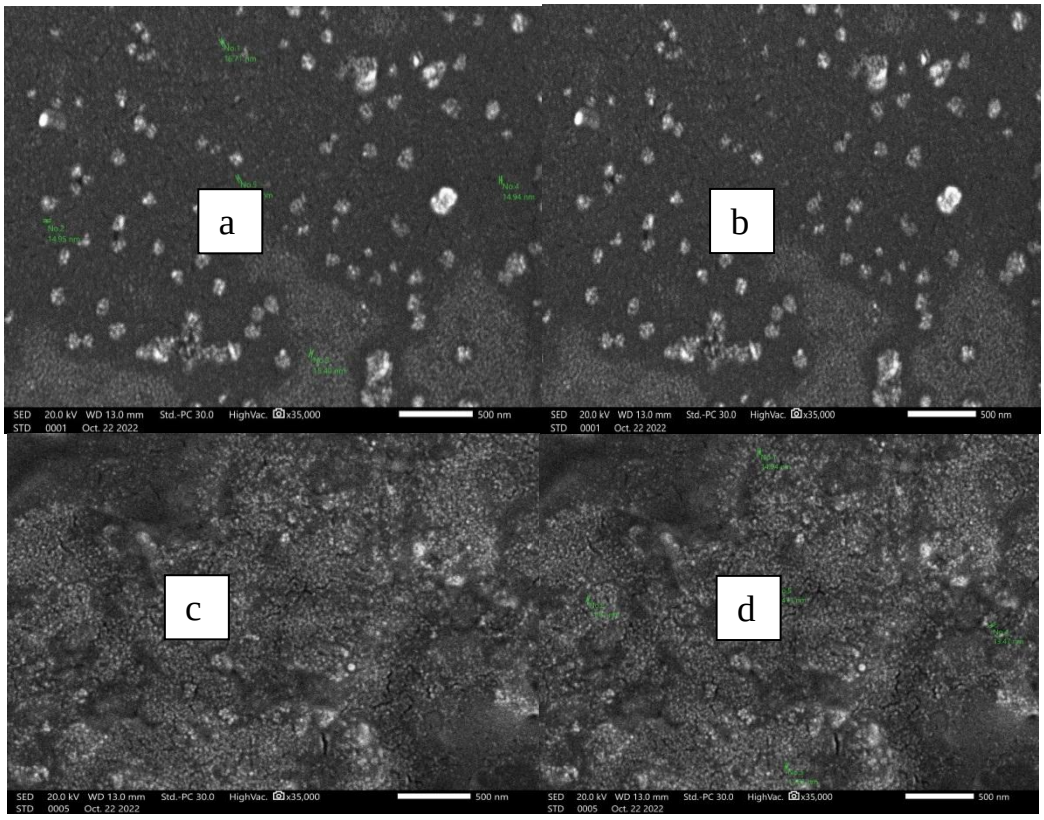

Fig.10. SEM images for HL (1); a,b and Zn(II) complex (11); c,d with different magnification

Fluorescence spectroscopy

The emission spectra of the ligand HL(1), Cu(II) complex **(6)**, Zn(II) complex (11) and Ag(I) complex (12) were recorded in DMF and were shown in Fig. 11. [62]. After an excitation

wavelength of 290 nm, the Cu (II) metal complex **(6)** showed an emission wavelength of 390 nm, and discovered to be red shifted. Furthermore, the red shift of the emission wavelength in the case of Cu (II) may be caused by the primary amino group. Additionally, the conjugation of the ligand and metal complex resulted in an increase in fluorescence intensity. The copper; Cu (II) metal complex has fluorescent in nature, as seen by the fluorescence emission spectra Fig. 11 (A) & (B).

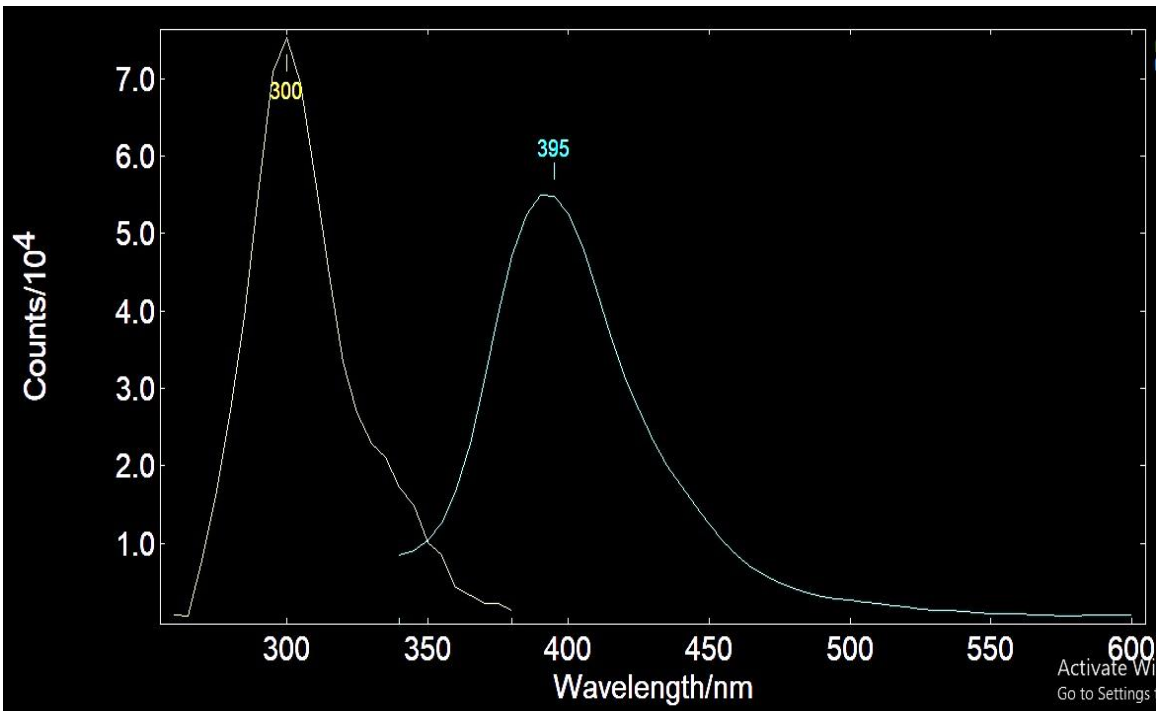

Fig.11 (A). Fluorescence spectroscopy of the ligand HL **(1)**

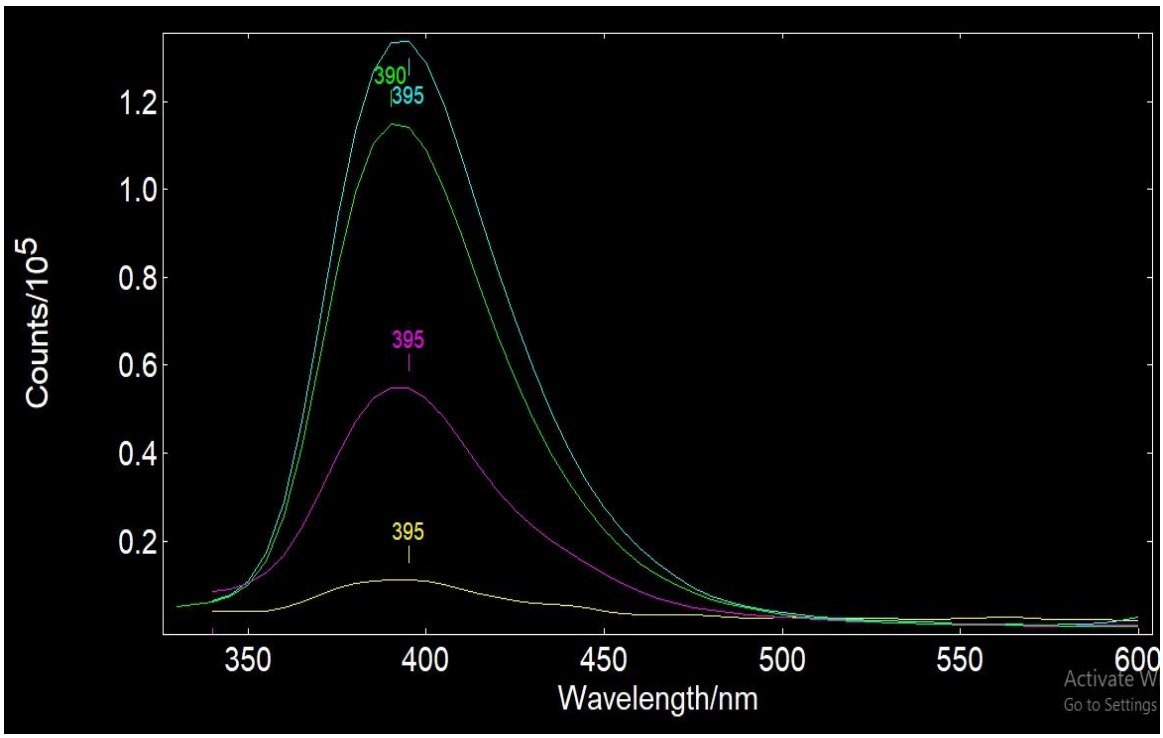

Fig.11 (B). Fluorescence spectroscopy of Cu (II) complex **(6)**, Zn (II) complex **(11)** and Ag (I) complex **(12)**

Chemotherapeutic Studies: Cytotoxic evolution against prostatic carcinoma cell line of the ligand and its complexes have been carried out. Ligand (1) and its complexes showed enhanced activity in comparison to the standard drug (Cisplatin) was applied with IC_{50} = *8.51-401.18 µg/ml* range. Zn (II) complex **(11)** was the most potent cytotoxic agent against prostatic carcinoma with IC_{50} = *8.51 µg/ml which candidates as anticancer agent.*

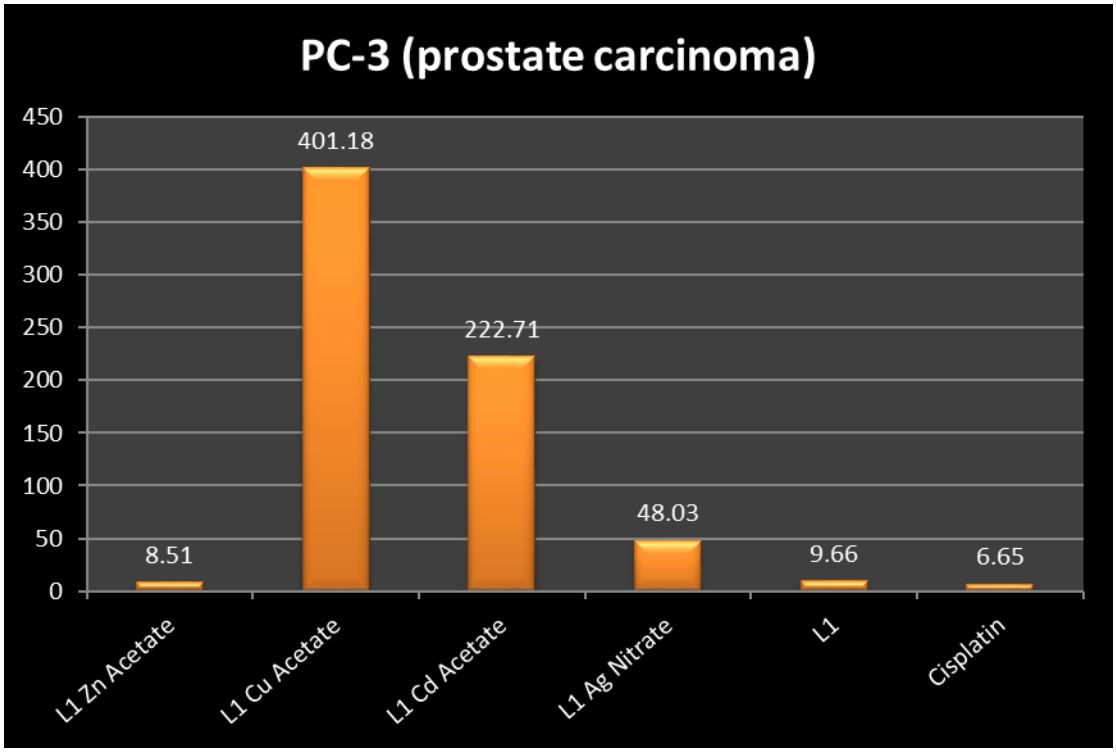

Fig. 12. IC_{50} values of the ligand, HL **(1)** and its metal complexes against human PC-3 cancer cell lines

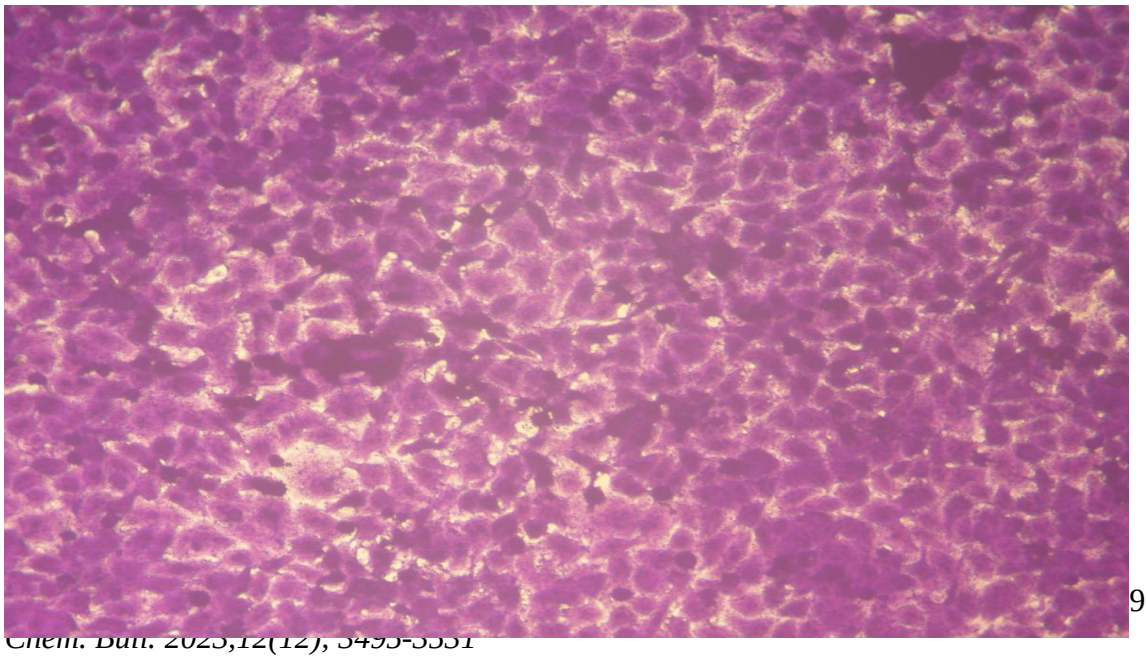

Fig (13). Photomicrograph showed non-treated PC-3 cells

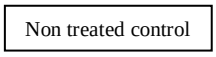

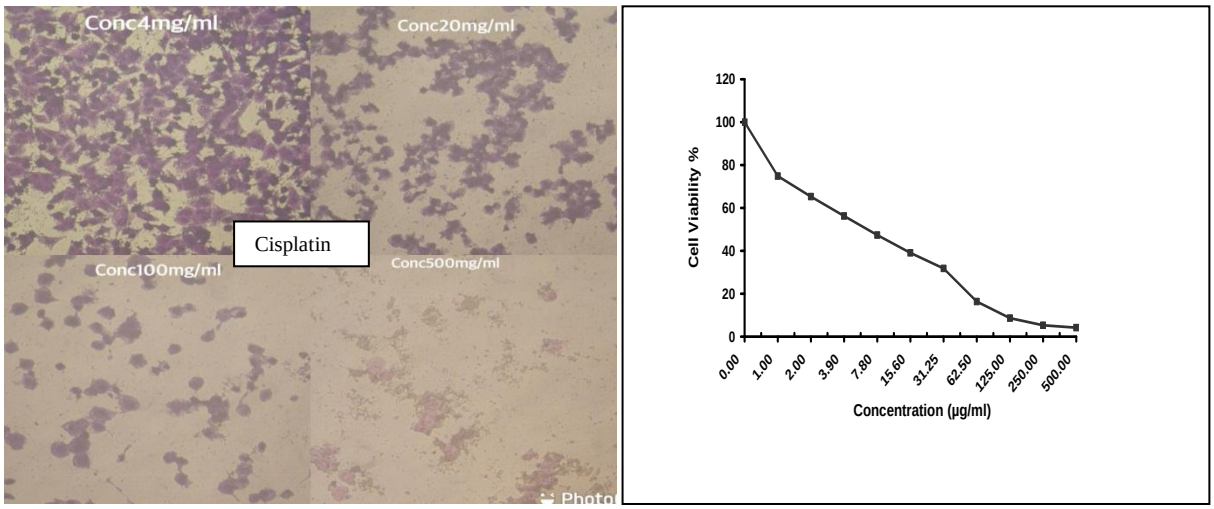

Fig(14). Photomicrograph showed the effect of standard drug (Cisplatin) against PC-3 cells at different concentrations

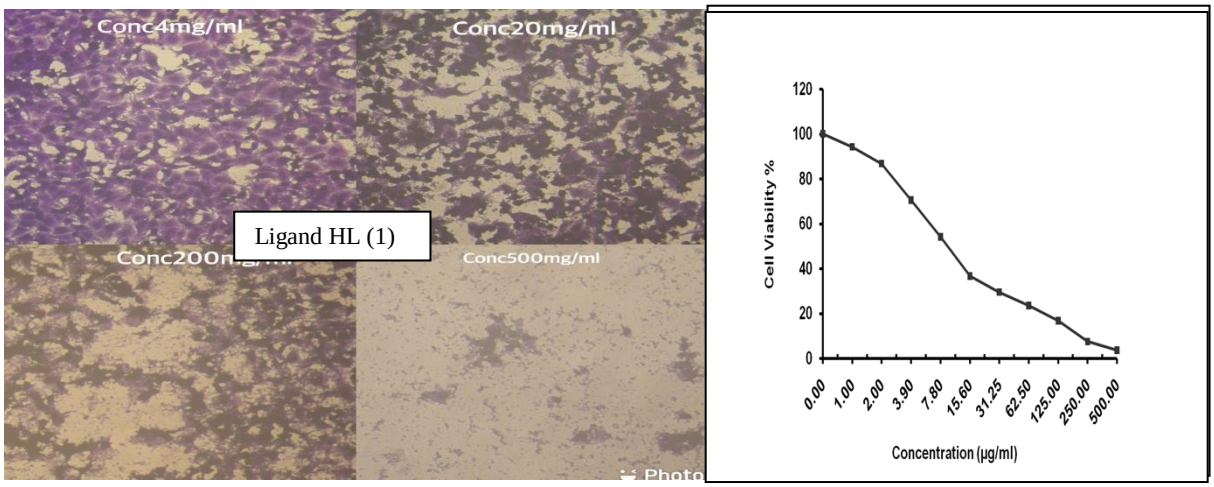

Fig(15). Photomicrograph showed the effect of Ligand HL **(1)** against PC-3 cells at different concentrations

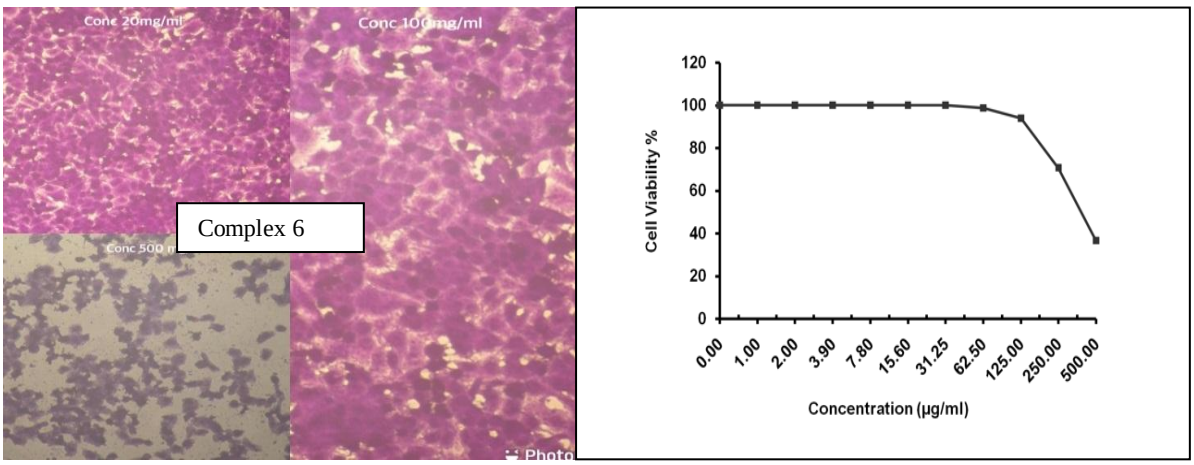

Fig(16). Photomicrograph showed the effect of complex **(6)** against PC-3 cells at different concentrations

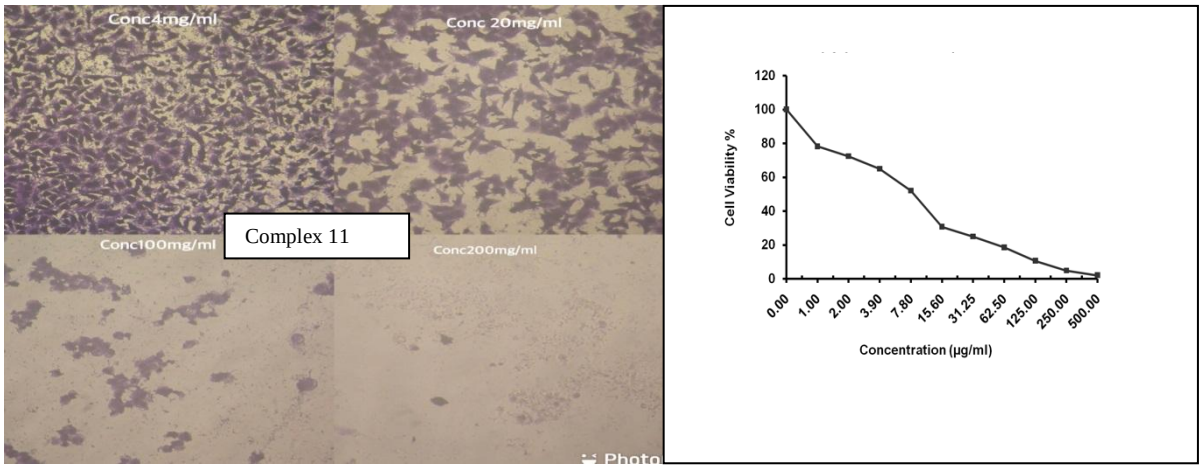

Fig(17) Photomicrograph showed the effect of complex **(11)** against PC-3 cells at different concentrations

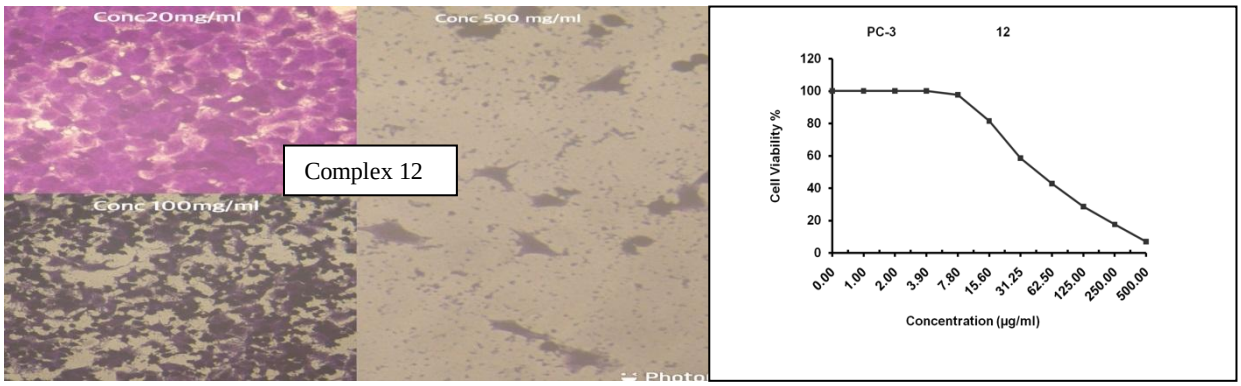

Fig(18) Photomicrograph showed the effect of complex **(12)** against PC-3 cells at different concentrations

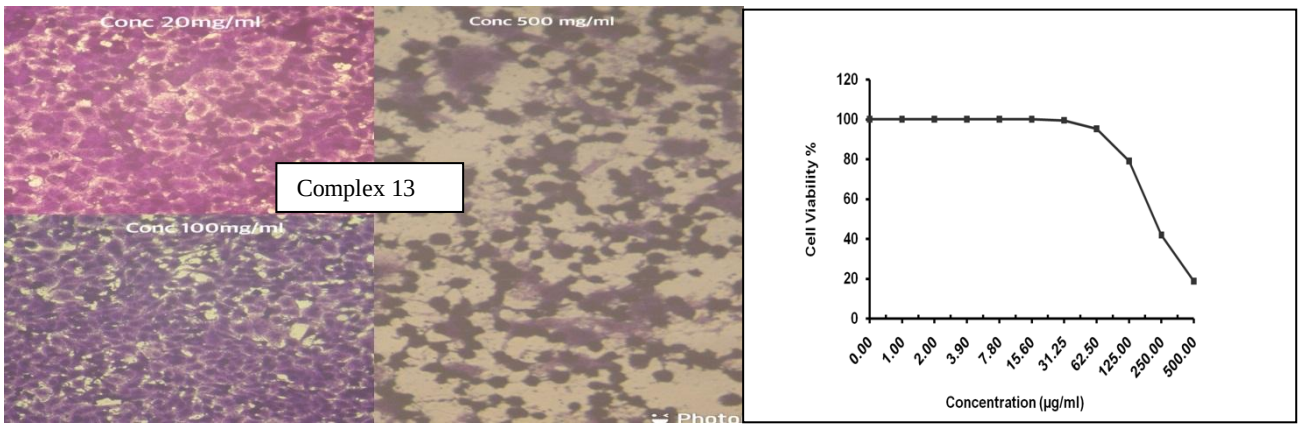

Fig(19) Photomicrograph showed the effect of complex **(13)** against PC 3 cells at different concentrations

Antimicrobial Activity

In vitro biological screening tests of the ligand and metal complexes **(1), (6), (11), (12)** and **(13)** carried out as antibacterial and antifungal activity and presented in table 5 and figure 12. The antibacterial activity was tested against two bacterial strains; Gram-positive and Gram-negative strains. The results compared with standard drug (Ampicllin (Gram positive) and Gentamicin (Gram negative). The data indicated that, complexes were active against bacteria. The results showed that the cytotoxic effect against Gram positive and Gram negative strains is Cd (II) complex **(13)** was high effect, for *E.coli* the order of cytotoxic effect was standard > complex **(11)** = complex **(13)** and others were zero effect. Complex **(1) , (6)** and **(12)** had no effect against Bacillus subtilis, Staphylococcus aurous, *E.coli, candida albicans* and Pseudomonas aeruginosa .Cd(II) complex showed wide range of bactericidal activities against the gram positive and gram negative bacteria. Further, the Cd (II) complex **(13)** was more active than the free ligand, which indicates that, metalation increases antimicrobial activity.

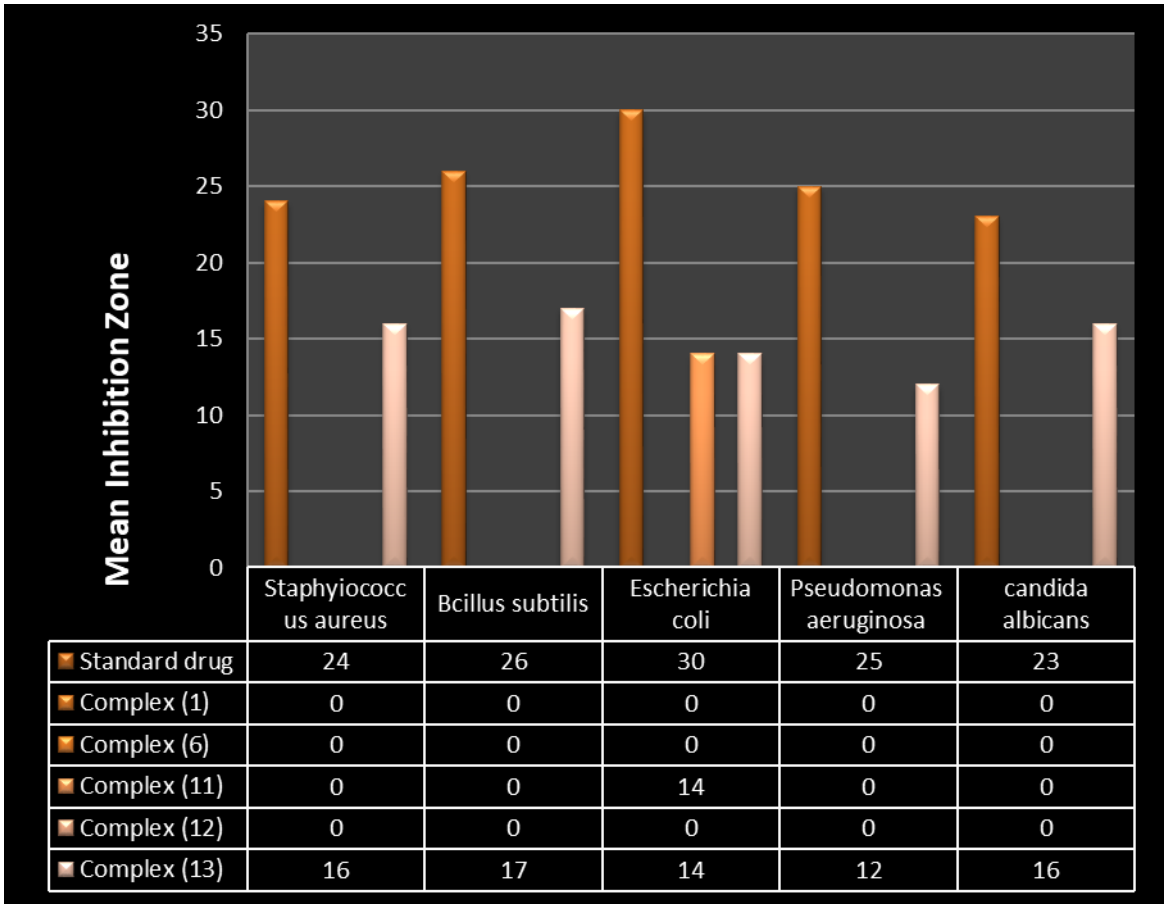

	Staphyiococcus aureus	Bcillus subtilis	Escherichia coli	Pseudomonas aeruginosa	candida albicans
Standard drug	24	26	30	25	23
Complex (1)	0	0	0	0	0
Complex (6)	0	0	0	0	0
Complex (11)	0	0	14	0	0
Complex (12)	0	0	0	0	0
Complex (13)	16	17	14	12	16

Fig (20). The micro-organisms were tested against the activity 10 mg /ml of the standard drug, complexes **(1)**, **(6)**, **(11)**, **(12)** and **(13)**

Conclusion

Metalloorganic complexes of Ca(II), Fe(III), Co(II), Ni(II), Cu(II), Zn(II), Ag(I), Cd(II), Hg(II) and Pb(II) with N-(4-aminophenyl)-2-hydroxybenzamide amide ligand have much potential as therapeutic and cytotoxic agents against Prostatic carcinoma cell line (PC-3). Specific examples involving the design of metal complexes as anticancer and antimicrobial agents have been synthesized and characterized by transmission electron microscope (TEM), Scanning electron microscope with EDEX, (mass, IR, UV-VIS and ESR) spectroscopy, XRD, as well as magnetic moments, conductance, elemental and thermal analyses. Molar conductance in DMF solution indicates that, the complexes are non-electrolytes. The ESR spectra of solid Cu (II) complex **(8)** showed isotropic type indicating an octahedral geometry with covalent bond character. X-ray Diffraction Spectroscopy XRD has been done. The XRD reveal that cu (II) complex **(6)**, Zn (II) complex **(11)** and Ag (I) complex **(12)** these complexes have the average crystallite sizes

of 27.1,22.6 and 7.11 nm respectively. It was suggested that the complexes were nanocrystalline. Cytotoxic evolution against Prostatic carcinoma cell line of the ligand and its complexes has been carried out. Ligand (1) and its complexes showed enhanced activity in comparison to the standard drug (Cisplatin) was applied with IC_{50} = *8.51-401.18 µg/ml* range. Zn(II) complex **(11)** was the most potent cytotoxic agent against prostatic carcinoma with IC_{50} = *8.51 µg/ml which candidates as anticancer agent. Antimicrobial activity also, had been carried out.* These organometallic compounds candidates as ant prostatic cancer agents.

Reference

1. Giri, V. N., Morgan, T. M., Morris, D. S., Berchuck, J. E., Hyatt, C., & Taplin, M. E. (2022). Genetic testing in prostate cancer management: Considerations informing primary care. *CA: A Cancer Journal for Clinicians*, *72*(4), 360-371.

2. Rahib, L., Wehner, M. R., Matrisian, L. M., & Nead, K. T. (2021). Estimated projection of US cancer incidence and death to 2040. *JAMA Network Open*, *4*(4), e214708-e214708.

3. Conti, D. V., Darst, B. F., Moss, L. C., Saunders, E. J., Sheng, X., Chou, A., ... & Strom, S. S. (2021). Trans-ancestry genome-wide association meta-analysis of prostate cancer identifies new susceptibility loci and informs genetic risk prediction. *Nature genetics*, *53*(1), 65-75.

4. Russo, J., & Giri, V. N. (2022). Germline testing and genetic counselling in prostate cancer. *Nature Reviews Urology*, *19*(6), 331-343.

5. Sekhoacha, M., Riet, K., Motloung, P., Gumenku, L., Adegoke, A., & Mashele, S. (2022). Prostate cancer review: Genetics, diagnosis, treatment options, and alternative approaches. *Molecules*, *27*(17), 5730.

6. Papachristodoulou, A., & Abate-Shen, C. (2022). Precision intervention for prostate cancer: re-evaluating who is at risk. *Cancer Letters*, *538*, 215709.

7. Vietri, M. T., D'Elia, G., Caliendo, G., Resse, M., Casamassimi, A., Passariello, L., ... & Molinari, A. M. (2021). Hereditary prostate cancer: genes related, target therapy and prevention. *International journal of molecular sciences*, *22*(7), 3753.

8. LeVee, A., Lin, C. Y., Posadas, E., Figlin, R., Bhowmick, N. A., Di Vizio, D., ... & Gong, J. (2021). Clinical utility of olaparib in the treatment of metastatic castration-resistant prostate cancer: a review of current evidence and patient selection. *OncoTargets and therapy*, 4819-4832.

9. Shekhar, S., Khan, A. M., Sharma, S., Sharma, B., & Sarkar, A. (2022). Schiff base metallodrugs in antimicrobial and anticancer chemotherapy applications: a comprehensive review. *Emergent Materials*, *5*(2), 279-293.

10. Jaros, S. W., Krogul-Sobczak, A., Bazanow, B., Florek, M., Poradowski, D., Nesterov, D. S., ... & Smoleński, P. (2021). Self-assembly and multifaceted bioactivity of a silver (I) quinolinate coordination polymer. *Inorganic Chemistry*, *60*(20), 15435-15444.

11. Zhang, H., Jiang, T., Zhang, J., & Huang, H. (2021). Catalytic reactions directed by a structurally well-defined aminomethyl cyclopalladated complex. *Accounts of Chemical Research*, *54*(23), 4305-4318.

12. El Tabl, A. S., Abu-Setta, M. H., Ashour, A. M., El-Afify, N. F., & Batakoushy, H. A. (2023). Organometallic ester compounds as a promising source of new antimicrobial drugs. *Egyptian Journal of Chemistry*.

13. El-Saber Batiha, G., Magdy Beshbishy, A., G. Wasef, L., Elewa, Y. H., A. Al-Sagan, A., Abd El-Hack, M. E., ... & Prasad Devkota, H. (2020). Chemical constituents and pharmacological activities of garlic (Allium sativum L.): A review. *Nutrients*, *12*(3), 872.

14. Braatz, D., Cherri, M., Tully, M., Dimde, M., Ma, G., Mohammadifar, E., ... & Haag, R. (2022). Chemical approaches to synthetic drug delivery systems for systemic applications. *Angewandte Chemie International Edition*, *61*(49), e202203942.

15. Jiang, Z., You, Q., & Zhang, X. (2019). Medicinal chemistry of metal chelating fragments in metalloenzyme active sites: A perspective. *European Journal of Medicinal Chemistry*, *165*, 172-197.

16. Nangare, S., & Patil, P. (2023). Black phosphorus nanostructure based highly sensitive and selective surface plasmon resonance sensor for biological and chemical sensing: a review. *Critical Reviews in Analytical Chemistry*, *53*(1), 1-26.

17. Liu, G. C., Li, Y., Chi, J., Xu, N., Wang, X. L., Lin, H. Y., & Chen, Y. Q. (2020). Multi-functional fluorescent responses of cobalt complexes derived from functionalized amide-bridged ligand. *Dyes and Pigments*, *174*, 108064.

18. Eliwa, E. M., Elgammal, W. E., Sharaf, M. H., Elsawy, M. M., Kalaba, M. H., El-Fakharany, E. M., ... & Abd El-Wahab, H. (2022). New Gd (I)/Cs (III) complexes of benzil-based thiocarbohydrazone macrocyclic ligand: chemical synthesis, characterization, and study their biological effectiveness as antibacterial, antioxidant, and antiviral additives for polyurethane surface coating. *Applied Organometallic Chemistry*, *36*(6), e6689.

19. Deh, K., Ponath, G. D., Molvi, Z., Parel, G. C. T., Gillen, K. M., Zhang, S., ... & Wang, Y. (2018). Magnetic susceptibility increases as diamagnetic molecules breakdown: Myelin digestion during multiple sclerosis lesion formation contributes to increase on QSM. *Journal of Magnetic Resonance Imaging*, *48*(5), 1281-1287.

20. Kamal, S., Khalid, M., Khan, M. S., & Shahid, M. (2023). Metal organic frameworks and their composites as effective tools for sensing environmental hazards: An up to date tale of mechanism, current trends and future prospects. *Coordination Chemistry Reviews*, *474*, 214859.

21. El-Apasery, M. A., Abdellatif, M. E., Yassin, F. A., & Ahmed, S. M. (2023). Synthesis of Novel Disperse Dyes based on Arylazophenols: Part 2. Anticancer Activities. *Egyptian Journal of Chemistry*, *66*(4), 49-53.

22. Wright, A. J. (2018). *Polymer Materials for the Encapsulation and Degradation of Chemical Warfare Agents*. University of Kent (United Kingdom).

23. Ibrahim, H., Bala, M. D., & Friedrich, H. B. (2022). Poly-functional imino-N-heterocyclic carbene ligands: Synthesis, complexation, and catalytic applications. *Coordination Chemistry Reviews*, *469*, 214652.

24. Abdou, S., Abd-El Wahed, M. M., & Abu-Setta, M. H. (2018). Metallo-bioactive compounds as potential novel anticancer therapy. *International Journal of Advances in Chemistry*, *4*(1), 17-37.

25. Selvaraj, S., Rajkumar, P., Kesavan, M., Gunasekaran, S., & Kumaresan, S. (2019). Experimental and theoretical analyzes on structural and spectroscopic properties of monomer and dimeric form of (S)-Piperidine-2-Carboxylic acid: An attempt on medicinal plant. *Vibrational Spectroscopy*, *100*, 30-39.

26. El-Ghamry, M. A., Elzawawi, F. M., Aziz, A. A. A., Nassir, K. M., & Abu-El-Wafa, S. M. (2022). New Schiff base ligand and its novel Cr (III), Mn (II), Co (II), Ni (II), Cu (II), Zn (II) complexes: Spectral investigation, biological applications, and semiconducting properties. *Scientific Reports*, *12*(1), 17942.

27. Begum, N., Mustaq, S., Aziz, S. S., & Arifuddin, M. (2021). Indian Journal of Advances in Chemical Science. *Indian Journal of Advances in Chemical Science*, *9*(3), 218-225.

28. El-Tabl, A. S., Ismail, A. E. H., Abd EL-Wahed, M. M., Sayed Ahmed, R. A., & Ashour, A. M. (2022). Novel nano-metal complexes of modified aspirin as future

antimicrobial agents. *International Journal of Pharmaceutical Research* (09752366), 14(1).

29. El-Tabl, A. S., Abd-El Wahed, M. M., Sayed Ahmed, R. A., Alhalib, A. A. A., & Ashour, A. M. (2022). Physico-chemical Characterization and Estimation of Antimicrobial Activity of Modified Aspirin in the form of Nano-organometallic Compounds. *Chemical Science International Journal*, 31(3), 11-37.

30. El Tabl, A. S., Abd-El Wahed, M. M., Ashour, A. M., Aly, A. A., Abu-Setta, M. H.H. (2023). Recent advances in metal complexes of new multifunctional ether ligand as potential anti-breast cancer agents. *European Chemical Bulletin, 12 (5),* 1436-1463.

31. Ali, S. G., El Tabl, A. S., Shabana, A. A., Abd-El Wahed, M. M., Ashour, A. M., Abu-Setta, M. H.H. & Elzaref A. S. (2023). Recent advances in metal complexes of new multifunctional ether ligand as potential anti-breast cancer agents. *European Chemical Bulletin, 12 (5),* 1464-1514

32. Kantcheva, M., & Ciftlikli, E. Z. (2002). FTIR Spectroscopic Characterization of NO x Species Adsorbed on ZrO2 and ZrO2− SO42. *The Journal of Physical Chemistry B*, *106*(15), 3941-3949.

33. Liu, Zeyu, Tian Lu, and Qinxue Chen. "An sp-hybridized all-carboatomic ring, cyclo [18] carbon: Electronic structure, electronic spectrum, and optical nonlinearity." *Carbon* 165 (2020): 461-467.

34. Griesar, K., & Haase, W. (2023). Magnetic properties of transition-metal-containing liquid crystals. In *Magnetic properties of organic materials* (pp. 325-344). Routledge.

35. Jiang, X., Liu, Q., Xing, J., Liu, N., Guo, Y., Liu, Z., & Zhao, J. (2021). Recent progress on 2D magnets: Fundamental mechanism, structural design and modification. *Applied Physics Reviews*, *8*(3).

36. Samy, F., & Shebl, M. (2020). Synthesis, spectroscopic, biological, and theoretical studies of new complexes from (E)-3-(2-(5, 6-diphenyl-1, 2, 4-triazin-3-yl) hydrazono) butan-2-one oxime. *Applied Organometallic Chemistry*, *34*(4), e5502.

37. Mohana Krishnudu, D., Sreeramulu, D., & Reddy, P. V. (2020). Alkali treatment effect: Mechanical, thermal, morphological, and spectroscopy studies on abutilon indicum fiber-reinforced composites. *Journal of Natural Fibers*, *17*(12), 1775-1784.

38. Melendez-Rodriguez, B., Torres-Giner, S., Zavagna, L., Sammon, C., Cabedo, L., Prieto, C., & Lagaron, J. M. (2021). Development and characterization of electrospun fiber-based poly (ethylene-co-vinyl alcohol) films of application interest as high-gas-barrier interlayers in food packaging. *Polymers*, *13*(13), 2061.

39. Dilissen, N., Vleugels, J., Vermeiren, J., García-Baños, B., Marín, J. R. S., & Catalá-Civera, J. M. (2023). Temperature dependency of the dielectric properties of hydrated and ordinary Portland cement and their constituent phases at 2.45 GHz up to 1100 C. *Cement and Concrete Research*, *165*, 107067.

40. Xie, B., Chen, J., Chen, J., Ma, C., Zhao, L., & Tchameni, A. P. (2023). Novel thermo-associating polymer/silica nanocomposite as a temperature-resistant rheology modifier for bentonite-free water-based drilling fluids. *Geoenergy Science and Engineering*, *222*, 211426.
41. Vasile, B. S., Dobra, G., Iliev, S., Cotet, L., Neacsu, I. A., Surdu, V. A & Filipescu, L. (2021). Thermally activated Al (OH) 3 part II—effect of different thermal treatments. *Ceramics*, *4*(4), 564-575.

42. Singh, N. K., Sharma, S., Krishnakumar, A., Choudhary, R. K., Kumbhar, A. A., Butcher, R. J., ... & Yadav, P. N. (2022). Exploration of anticancer potency of N (4) thiomorpholinyl isatin/5-haloisatin thiosemicarbazones on coordination to Cu2+ ion. *Inorganic Chemistry Communications*, *143*, 109767.

43. Wang, L., Li, Z., Wu, Q., Huang, Z., Yuan, L., Chai, Z., & Shi, W. (2020). Layered structure-based materials: challenges and opportunities for radionuclide sequestration. *Environmental Science: Nano*, *7*(3), 724-752.

44. Do Prado, M. V., González, B., Vicente, M. A., Trujillano, R., Nassar, E. J., Gil, A., & Ciuffi, K. J. (2023). Multifunctional heterogeneous catalysts: Tetrakis (pentafluorophenyl) porphinato] iron (III) immobilized on amine–functionalized Diatomaceous Earth for catalytic and adsorption applications. *Journal of Environmental Chemical Engineering*, *11*(3), 109729.

45. Almagul, U., Shah, A., & Zhazira, B. (2020). Studies on Valued Components Extraction from Titanium-Magnesium Production Wastes. *Journal of Advanced Research in Fluid Mechanics and Thermal Sciences*, *75*(3), 140-155.

46. Pei, S., You, S., Ma, J., Chen, X., & Ren, N. (2020). Electron spin resonance evidence for electro-generated hydroxyl radicals. *Environmental Science & Technology*, *54*(20), 13333-13343.

47. El-Tabl, Abdou S., Mohamed Tawfek Shaban, and Noran Mohamed Abd El-Wahed. "Novel metal complexes as antimicrobial agents, synthesis and spectroscopic characterization." *Journal of Chemistry and Chemical Sciences* 9.3 (2019): 74-108.

48. Barba, F. J., Roohinejad, S., Ishikawa, K., Leong, S. Y., Bekhit, A. E. D. A., Saraiva, J. A., & Lebovka, N. (2020). Electron spin resonance as a tool to monitor the

influence of novel processing technologies on food properties. *Trends in Food Science & Technology*, *100*, 77-87.

49. Delgado, F., & Lorente, N. (2021). A theoretical review on the single-impurity electron spin resonance on surfaces. *Progress in Surface Science*, *96*(2), 100625.

50. Zhang, X., Wolf, C., Wang, Y., Aubin, H., Bilgeri, T., Willke, P., ... & Choi, T. (2022). Electron spin resonance of single iron phthalocyanine molecules and role of their non-localized spins in magnetic interactions. *Nature Chemistry*, *14*(1), 59-65.

51. Chiappinelli, A., Mangiacotti, M., Tomaiuolo, M., Trotta, G., Marchesani, G., & Chiaravalle, A. E. (2019). Identification of X-ray-irradiated hazelnuts by electron spin resonance (ESR) spectroscopy. *European Food Research and Technology*, *245*(10), 2323-2329.

52. King, G. E., Tsukamoto, S., Herman, F., Biswas, R. H., Sueoka, S., & Tagami, T. (2020). Electron spin resonance (ESR) thermochronometry of the Hida range of the Japanese Alps: validation and future potential. *Geochronology*, *2*(1), 1-15.
53. Jiang, S., Xie, Y., Li, M., Guo, Y., Cheng, Y., Qian, H., & Yao, W. (2020). Evaluation on the oxidative stability of edible oil by electron spin resonance spectroscopy. *Food chemistry*, *309*, 125714.

54. Hwang, J., Krylov, D., Elbertse, R., Yoon, S., Ahn, T., Oh, J., ... & Bae, Y. (2022). Development of a scanning tunneling microscope for variable temperature electron spin resonance. *Review of Scientific Instruments*, *93*(9).

55. Willke, P., Singha, A., Zhang, X., Esat, T., Lutz, C. P., Heinrich, A. J., & Choi, T. (2019). Tuning single-atom electron spin resonance in a vector magnetic field. *Nano Letters*, *19*(11), 8201-8206.

56. Moro, F., Ke, S., del Águila, A. G., Söll, A., Sofer, Z., Wu, Q., ... & Fanciulli, M. (2022). Revealing 2D Magnetism in a Bulk CrSBr Single Crystal by Electron Spin Resonance. *Advanced Functional Materials*, *32*(45), 2207044.

57. Gálvez, J. R., Wolf, C., Delgado, F., & Lorente, N. (2019). Cotunneling mechanism for all-electrical electron spin resonance of single adsorbed atoms. *Physical Review B*, *100*(3), 035411.

58. Singamaneni, S. R., Martinez, L. M., Niklas, J., Poluektov, O. G., Yadav, R., Pizzochero, M., ... & McGuire, M. A. (2020). Light induced electron spin resonance properties of van der Waals CrX3 (X= Cl, I) crystals. *Applied Physics Letters*, *117*(8).
59. Thakar, M. A., Jha, S. S., Phasinam, K., Manne, R., Qureshi, Y., & Babu, V. H. (2022). X ray diffraction (XRD) analysis and evaluation of antioxidant activity of

copper oxide nanoparticles synthesized from leaf extract of Cissus vitiginea. *Materials Today: Proceedings*, *51*, 319-324.

60. Relucenti, M., Familiari, G., Donfrancesco, O., Taurino, M., Li, X., Chen, R., ... & Selan, L. (2021). Microscopy methods for biofilm imaging: focus on SEM and VP-SEM pros and cons. *Biology*, *10*(1), 51.

61. El-Tabl, A.S., Abd-El Wahed, M. M., Abu-Setta, M.H.H., El-Mahsarawy, A.I., & Ashour, A.M (2022). Cytotoxicity and antitumor activity of organometallic copper (II) Nano particles in a chemically induced hepatocellular carcinoma rat model. *International Journal of Pharmaceutical Sciences and Research*, Vol.14 (3): 1000-11

62. Hassoun, A. (2021). Exploring the potential of fluorescence spectroscopy for the discrimination between fresh and frozen-thawed muscle foods. *Photochem*, *1*(2), 247-263.